

## Improving the hot-spot pressure and demonstrating ignition hydrodynamic equivalence in cryogenic deuterium–tritium implosions on OMEGAa)

V. N. Goncharov, T. C. Sangster, R. Betti, T. R. Boehly, M. J. Bonino, T. J. B. Collins, R. S. Craxton, J. A. Delettrez, D. H. Edgell, R. Epstein, R. K. Follett, C. J. Forrest, D. H. Froula, V. Yu. Glebov, D. R. Harding, R. J. Henchen, S. X. Hu, I. V. Igumenshchev, R. Janezic, J. H. Kelly, T. J. Kessler, T. Z. Kosc, S. J. Loucks, J. A. Marozas, F. J. Marshall, A. V. Maximov, R. L. McCrory, P. W. McKenty, D. D. Meyerhofer, D. T. Michel, J. F. Myatt, R. Nora, P. B. Radha, S. P. Regan, W. Seka, W. T. Shmayda, R. W. Short, A. Shvydky, S. Skupsky, C. Stoeckl, B. Yaakobi, J. A. Frenje, M. Gatu-Johnson, R. D. Petrasso, and D. T. Casey

Citation: *Physics of Plasmas* (1994-present) **21**, 056315 (2014); doi: 10.1063/1.4876618

View online: <http://dx.doi.org/10.1063/1.4876618>

View Table of Contents: <http://scitation.aip.org/content/aip/journal/pop/21/5?ver=pdfcov>

Published by the *AIP Publishing*

---

### Articles you may be interested in

[Nuclear imaging of the fuel assembly in ignition experimentsa\)](#)

*Phys. Plasmas* **20**, 056320 (2013); 10.1063/1.4807291

[Improving cryogenic deuterium–tritium implosion performance on OMEGAa\)](#)

*Phys. Plasmas* **20**, 056317 (2013); 10.1063/1.4805088

[Detailed implosion modeling of deuterium-tritium layered experiments on the National Ignition Facilitya\)](#)

*Phys. Plasmas* **20**, 056318 (2013); 10.1063/1.4802194

[Solid debris collection for radiochemical diagnostics at the National Ignition Facilitya\)](#)


*Rev. Sci. Instrum.* **83**, 10D904 (2012); 10.1063/1.4732856

[Robustness studies of ignition targets for the National Ignition Facility in two dimensionsa\)](#)

*Phys. Plasmas* **15**, 056305 (2008); 10.1063/1.2890123

---

A collection of Pfeiffer Vacuum industrial equipment, including a red turbopump, a silver turbopump, a silver backing pump, a red turbopump with a long shaft, and a silver chamber component.

 Vacuum Solutions from a Single Source

- Turbopumps
- Backing pumps
- Leak detectors
- Measurement and analysis equipment
- Chambers and components

**PFEIFFER**  **VACUUM**

# Improving the hot-spot pressure and demonstrating ignition hydrodynamic equivalence in cryogenic deuterium–tritium implosions on OMEGA<sup>a)</sup>

V. N. Goncharov,<sup>1,b),c)</sup> T. C. Sangster,<sup>1</sup> R. Betti,<sup>1,d)</sup> T. R. Boehly,<sup>1</sup> M. J. Bonino,<sup>1</sup> T. J. B. Collins,<sup>1</sup> R. S. Craxton,<sup>1</sup> J. A. Delettrez,<sup>1</sup> D. H. Edgell,<sup>1</sup> R. Epstein,<sup>1</sup> R. K. Follett,<sup>1,e)</sup> C. J. Forrest,<sup>1</sup> D. H. Froula,<sup>1,e)</sup> V. Yu. Glebov,<sup>1</sup> D. R. Harding,<sup>1</sup> R. J. Henchen,<sup>1,e)</sup> S. X. Hu,<sup>1</sup> I. V. Igumenshchev,<sup>1</sup> R. Janezic,<sup>1</sup> J. H. Kelly,<sup>1</sup> T. J. Kessler,<sup>1</sup> T. Z. Kosc,<sup>1</sup> S. J. Loucks,<sup>1</sup> J. A. Marozas,<sup>1</sup> F. J. Marshall,<sup>1</sup> A. V. Maximov,<sup>1</sup> R. L. McCrory,<sup>1,d)</sup> P. W. McKenty,<sup>1</sup> D. D. Meyerhofer,<sup>1,d)</sup> D. T. Michel,<sup>1</sup> J. F. Myatt,<sup>1</sup> R. Nora,<sup>1,e)</sup> P. B. Radha,<sup>1</sup> S. P. Regan,<sup>1</sup> W. Seka,<sup>1</sup> W. T. Shmayda,<sup>1</sup> R. W. Short,<sup>1</sup> A. Shvydky,<sup>1</sup> S. Skupsky,<sup>1</sup> C. Stoeckl,<sup>1</sup> B. Yaakobi,<sup>1</sup> J. A. Frenje,<sup>2</sup> M. Gatu-Johnson,<sup>2</sup> R. D. Petrasso,<sup>2</sup> and D. T. Casey<sup>3</sup>

<sup>1</sup>Laboratory for Laser Energetics, University of Rochester, Rochester, New York 14623, USA

<sup>2</sup>Massachusetts Institute of Technology, Plasma Science and Fusion Center, Cambridge, Massachusetts 02139, USA

<sup>3</sup>Lawrence Livermore National Laboratory, Livermore, California 94551, USA

(Received 11 December 2013; accepted 15 April 2014; published online 23 May 2014)

Reaching ignition in direct-drive (DD) inertial confinement fusion implosions requires achieving central pressures in excess of 100 Gbar. The OMEGA laser system [T. R. Boehly *et al.*, *Opt. Commun.* **133**, 495 (1997)] is used to study the physics of implosions that are hydrodynamically equivalent to the ignition designs on the National Ignition Facility (NIF) [J. A. Paisner *et al.*, *Laser Focus World* **30**, 75 (1994)]. It is shown that the highest hot-spot pressures (up to 40 Gbar) are achieved in target designs with a fuel adiabat of  $\alpha \simeq 4$ , an implosion velocity of  $3.8 \times 10^7$  cm/s, and a laser intensity of  $\sim 10^{15}$  W/cm<sup>2</sup>. These moderate-adiabat implosions are well understood using two-dimensional hydrocode simulations. The performance of lower-adiabat implosions is significantly degraded relative to code predictions, a common feature between DD implosions on OMEGA and indirect-drive cryogenic implosions on the NIF. Simplified theoretical models are developed to gain physical understanding of the implosion dynamics that dictate the target performance. These models indicate that degradations in the shell density and integrity (caused by hydrodynamic instabilities during the target acceleration) coupled with hydrodynamics at stagnation are the main failure mechanisms in low-adiabat designs. To demonstrate ignition hydrodynamic equivalence in cryogenic implosions on OMEGA, the target-design robustness to hydrodynamic instability growth must be improved by reducing laser-coupling losses caused by cross beam energy transfer. © 2014 AIP Publishing LLC. [<http://dx.doi.org/10.1063/1.4876618>]

## I. INTRODUCTION

To ignite the deuterium–tritium (DT) fuel in an inertial confinement fusion<sup>1,2</sup> (ICF) implosion, the ion temperature and areal density of the central, lower-density region (hot spot) of the compressed DT fuel assembly must be sufficient to create self-heating by alpha particles produced as a result of fusing D and T. A typical ICF target consists of a higher-density shell filled with a lower-density fuel vapor. The shell has outer layers of ablator materials and an inner layer of frozen DT fuel. To compress the main fuel and initiate burn, the shell is accelerated inward by a temporally shaped pressure drive created by laser energy that is delivered either directly

to the target (direct drive) or indirectly by conversion to x rays inside a hohlraum (indirect drive).<sup>1,2</sup>

The peak hot-spot pressure is a critical parameter in ICF implosions. It determines the minimum shell kinetic energy required to create an igniting hot spot. This follows from a simple argument<sup>2</sup> that if the shell kinetic energy,  $E_k$ , is converted into the internal energy of the hot spot at stagnation,  $E_k \rightarrow p_{\max} R_{\text{hs}}^3$ , then  $E_k \sim (\rho R_{\text{hs}})^3 T^3 / p_{\max}^2$ , where  $R_{\text{hs}}$ ,  $p_{\max} \sim \rho T / m_i$ ,  $\rho$ , and  $T$  are the hot-spot radius, the maximum pressure, mass density, and temperature, respectively, and  $m_i$  is the average ion mass. Since the hot spot must satisfy<sup>1–3</sup>

$$(\rho R_{\text{hs}}) \times T \gtrsim 0.3 \text{ g/cm}^2 \times 5 \text{ keV} \quad (1)$$

to ignite (this fixes  $\rho R_{\text{hs}} T$  in the expression for the kinetic energy), the fuel kinetic energy must exceed a threshold value,  $E_k > E_{k,\text{min}}$ , which depends on the peak pressure

$$E_{k,\text{min}} \sim p_{\max}^{-2}. \quad (2)$$

Equation (2) shows that achieving higher pressures in the hot spot relaxes the requirement for the shell kinetic energy and laser drive energy.

<sup>a)</sup>Paper GI3 1, *Bull. Am. Phys. Soc.* **58**, 104 (2013).

<sup>b)</sup>Invited speaker.

<sup>c)</sup>Also at Department of Mechanical Engineering, University of Rochester, Rochester, New York 14623, USA.

<sup>d)</sup>Also at Department of Mechanical Engineering, University of Rochester, Rochester, New York 14623, USA and Department of Physics and Astronomy, University of Rochester, Rochester, New York 14623, USA.

<sup>e)</sup>Also at Department of Physics and Astronomy, University of Rochester, Rochester, New York 14623, USA.

Equation (1) sets the requirement for the hot-spot pressure in an igniting target. Since  $p = (1 + Z)\rho T/m_i$  (for DT fuel,  $Z = 1$  is the ion charge,  $m_i \simeq 2.5 m_p$ , and  $m_p$  is proton mass), Eq. (1) gives

$$p_{\text{hs}} > 200 \text{ Gbar} \left( \frac{50 \text{ } \mu\text{m}}{R_{\text{hs}}} \right). \quad (3)$$

The peak pressure also determines the neutron yield for sub-igniting ICF implosions. Indeed, the DT fusion reaction rate is  $dn_i/dt \sim V_{\text{hs}} \times n_i^2 \times \langle \sigma v \rangle$  and the reaction cross section scales as  $\langle \sigma v \rangle \sim T^{4.5}$  (at temperatures  $T \sim 2$  to 4 keV, which are typical for sub-ignition ICF implosions). Here,  $n_i$  is the ion density and  $V_{\text{hs}}$  is the hot-spot volume. This leads to the total neutron yield of

$$Y \sim V_{\text{hs}} \times p_{\text{max}}^2 \times T^{2.5} \times \Delta t_{\text{burn}}, \quad (4)$$

where  $\Delta t_{\text{burn}}$  is the burn duration. Using the adiabatic condition for the hot spot (Refs. 3 and 4)  $p \sim V_{\text{hs}}^{-5/3}$  (see also the discussion later in the text), Eq. (4) becomes

$$Y \sim p_{\text{max}}^{7/5} \times T^{2.5} \times \Delta t_{\text{burn}}. \quad (5)$$

Equation (5) shows that higher hot-spot pressures lead to higher target yields.

The maximum pressure depends mainly on the following two effects: first, the conversion efficiency of the shell kinetic energy into the hot-spot internal energy at shell stagnation, and second, the hot-spot size, since larger hot-spot volumes lead to smaller peak pressures for a given hot-spot internal energy  $E_{\text{int}}$ ,  $p_{\text{max}} \sim E_{\text{int}}/V_{\text{hs}}$ .

The first effect depends on the fraction of shell mass that stagnates at peak compression. At the beginning of shell deceleration [see Fig. 1(a)], the pressure of the central vapor region of an imploding target (which, together with the fuel ablated from the inside of the shell during deceleration, forms a hot spot at peak compression) exceeds the shell pressure and an outgoing shock wave is formed at the inner edge of the shell. The vapor (hot-spot) pressure increases, while the inner part of the shell converges and performs  $p dV$  work on the vapor region. The inward shell motion is limited by the deceleration force caused by the pressure gradient in the shock-compressed region [see Fig. 1(b)]. This pressure gradient is determined, first, by the pressure behind the shock front  $p_{\text{shock}}$  [which depends on density  $\rho$  and velocity  $v$  of the incoming shell (unshocked shell) ahead of the shock,  $p_{\text{shock}} \sim \rho v^2$ ] and, second, by the hot-spot pressure, which depends on the hot-spot convergence ratio  $p_{\text{hs}} \sim V_{\text{hs}}^{-5/3}$ . If two implosions are considered where the shells have different  $\rho v^2$ , the pressure behind the shock is lower and the pressure gradient (for a given hot-spot volume) is higher in the shell with a smaller  $\rho v^2$ . This shell, therefore, experiences a stronger deceleration force, leading to a larger hot-spot volume at stagnation. The amount of shell material overtaken by the outgoing shock is smaller in this case, resulting in a reduced fraction of the shell kinetic energy being converted into hot-spot internal energy. Since the shell deceleration rate depends on the density of the incoming shell, excessive decompression of the shell resulted from either the

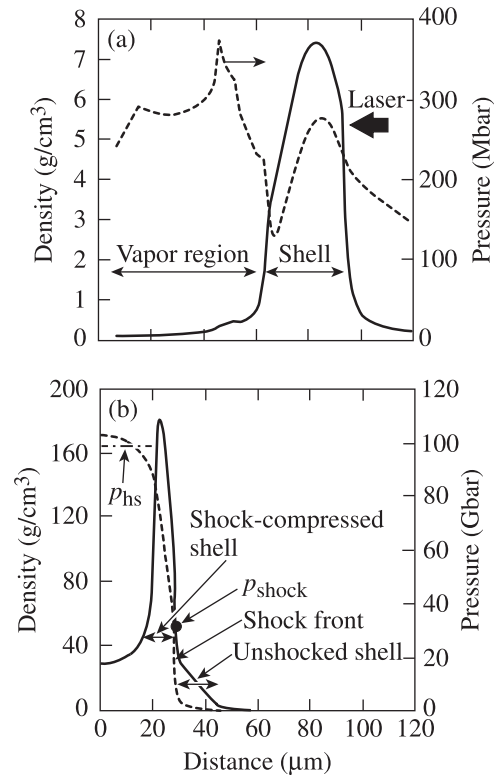


FIG. 1. The mass density (solid lines, left axes) and the pressure (dashed lines, right axes) profiles at the beginning of shell deceleration (a) and at the maximum hot-spot compression (b) for OMEGA cryogenic targets.

Rayleigh-Taylor (RT) instability growth<sup>5,6</sup> or preheat caused by radiation or suprathermal electrons must be prevented.

Predicting the evolution of the hot-spot pressure using hydrodynamic code simulations requires accurate modeling of many physical processes that take place during the target implosion. It is essential, therefore, to validate code predictions of key target-performance characteristics at each stage of the implosion against experimental data. In addition, experiments can help to identify new physical phenomena (not included in the code simulations) that limit target performance. For such purposes, cryogenic DT capsules are being imploded on the OMEGA Laser System<sup>7</sup> using direct-drive laser illumination. The targets are 7.3- to 12- $\mu\text{m}$ -thick deuterated plastic (CD) shells with outer diameters of 860  $\mu\text{m}$  and 40- to 65- $\mu\text{m}$ -thick cryogenic DT layers. Currently, the cryogenic fuel has the H/D/T ratios of 4%/56%/40%. Installing isotope separator on OMEGA in the upcoming year will allow to eliminate H and increase the D/T ratio to 50%/50%. These targets are driven using single- and multiple-picket pulses<sup>8</sup> with UV laser energies of 23 to 27 kJ at a peak intensity of 0.4 to  $1 \times 10^{15}$  W/cm<sup>2</sup>, reaching implosion velocities (defined as the peak mass-averaged shell velocity) of 2.2 to  $4 \times 10^7$  cm/s.

This paper describes recent progress in understanding cryogenic implosion performance on OMEGA. It is organized as follows: Section II describes the cryogenic target designs and the experiments carried out to validate one-dimensional (1-D) implosion parameters. Target performance is discussed in Sec. III; hydrodynamic modeling results are presented in Sec. IV. The performance degradation

mechanisms are discussed in Sec. V, and strategies for demonstrating ignition hydrodynamic equivalence on OMEGA are presented in Sec. VI. Conclusions are given in Sec. VII.

## II. TARGET DESIGNS AND VALIDATION OF 1-D IMPLOSION PARAMETERS

This section describes the cryogenic target designs and discusses the experimental campaigns carried out on OMEGA to validate the key predicted implosion parameters. The simulation results discussed in this section are obtained using the one-dimensional hydrocode *LILAC*.<sup>9</sup> These simulations include nonlocal electron thermal transport<sup>10</sup> and the cross-beam energy transfer (CBET) model.<sup>11–13</sup>

The compression of cryogenic DT fuel is studied for shell adiabat values in a range  $1.5 < \alpha < 6$ , [the adiabat,  $\alpha$ , is defined as the ratio of the shell pressure to the Fermi-degenerate pressure at the shell density (see Sec. III for more details)], and for various implosion velocities and peak laser intensities. The implosion velocity is controlled by varying the CD thickness from 7.2 to 12  $\mu\text{m}$  and the ice thickness from 40 to 65  $\mu\text{m}$ .

Two representative OMEGA cryogenic target designs are shown in Fig. 2. The fuel adiabat and the in-flight aspect ratio (IFAR) are controlled by changing the energies and separation of intensity pickets ahead of the main drive pulse. The lower-adiabat design, shown with a dashed line in Fig. 2, uses lower-intensity pickets. The shocks launched by lower laser intensities are weaker and travel slower across the shell. To ensure that the shocks launched by the pickets and the rise of the main pulse merge in close proximity to the inner surface of the shell requires larger temporal separations of the pickets in the lower-adiabat designs.

The plastic overcoat is ablated during the main drive pulse either fully or partially, depending on its thickness. For a given laser energy, there is an optimum CD layer thickness that maximizes the drive (ablation) pressure. This is determined by the interplay of the laser absorption efficiency, radiation losses, electron thermal conduction from the laser absorption region to the ablation front, and ablation efficiency.

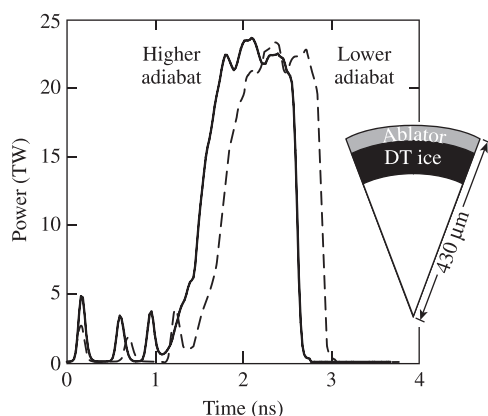


FIG. 2. Lower- (dashed line) and higher- (solid line) adiabat OMEGA cryogenic designs. The fuel adiabat and the shell in-flight aspect ratio are controlled by changing the energies and separation of the laser intensity pickets. The inset shows target dimensions.

The inverse bremsstrahlung **absorption**<sup>2</sup> is proportional to the average square of the ion charge  $\langle Z^2 \rangle$ . Consequently, having CD plasma in the laser-deposition region is beneficial for the overall laser absorption because  $\langle Z^2 \rangle_{\text{CD}} / \langle Z^2 \rangle_{\text{DT}} \simeq 18.5$ . The higher absorption also leads to a larger coronal temperature and an increased threshold for the two-plasmon decay (TPD) instability.<sup>14–16</sup> Furthermore, the higher average ion charge  $\langle Z \rangle$  and the low fraction of hydrogen atoms in the plasma corona give an additional reduction in TPD growth because of the lower damping rates of ion-acoustic waves.<sup>17</sup> A thicker CD layer also shields the main fuel against radiation preheat from the plasma corona (despite the small opacity of DT, calculations indicate that the amount of radiation from the plasma corona absorbed in the main fuel is sufficient to raise the fuel adiabat by 30% to 50% during target acceleration).

Using ablator materials with higher  $\langle Z^2 \rangle$ , on the other hand, leads to larger **radiation losses**. Higher- $Z$  materials also reduce the **heat conduction** from the plasma region where laser energy is absorbed to the ablation front, since the thermal conductivity is proportional to  $\langle Z \rangle / \langle Z^2 \rangle$ . This reduces the mass ablation rate and the ablation pressure.

The **mass-ablation efficiency** (the ablated shell mass per unit area and unit time for a given absorbed laser energy), which depends on the ratio of atomic weight  $A$  and the averaged ion charge  $\langle Z \rangle$ , is higher in DT. This dependence follows from the steady-state ablation model,<sup>18</sup> where the incoming absorbed laser power flux (laser intensity)  $I$  is balanced by the outgoing energy flux of expanding plasma flow,  $\rho v^3$ . Here,  $\rho$  is the plasma mass density and  $v$  is the expansion velocity at the location of the laser-energy deposition. Such a model predicts the ablation-pressure and the mass-ablation-rate scalings to be  $p_a \sim I^{2/3} (A/Z)^{1/3}$  and  $\dot{m} \sim I^{1/3} (A/Z)^{2/3}$ , respectively. Since  $(A/Z)_{\text{DT}} / (A/Z)_{\text{CD}} \simeq 1.25$ , the ablation pressure and mass ablation rate, as fractions of the absorbed laser energy, are higher in DT by 8% and 16%, respectively.

Considering these competing effects, the ablation pressure in cryogenic direct-drive implosions is maximized if the laser energy of the main pulse is absorbed in the ablated CD plasma, while DT is being ablated from the higher-density part of the shell. Such an arrangement is possible because the ablation and absorption regions are spatially separated. For an OMEGA-scale laser system, this leads to the optimum CD thickness of  $\sim 7.5$  to 8  $\mu\text{m}$ . Figure 3 plots the ablation pressure as a function of the CD thickness for targets with a fixed shell mass and a varying ratio of CD to DT layer thicknesses. The empty squares in the figure represent the ablation pressure calculated at the beginning of the shell acceleration, and the solid circles show pressures when the shells have converged by factor of 2.5. The CD thickness that maximizes the ablation pressure changes from  $\sim 6 \mu\text{m}$  earlier in the pulse to 7.5  $\mu\text{m}$  at later times. This change occurs because the CD layers thicker than 6.5  $\mu\text{m}$  are still being ablated at earlier times, resulting in a lower rocket efficiency (shell kinetic energy per unit incident laser energy). By the time the shell has converged by a factor of 2.5, the CD layers thinner than  $\sim 10 \mu\text{m}$  are completely ablated, resulting in an increased rocket efficiency. If the initial CD thickness is less than 7  $\mu\text{m}$ , however, the ablated DT plasma expands into the



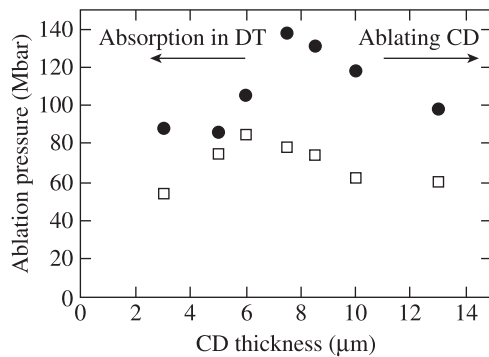


FIG. 3. Simulated ablation pressure versus the initial CD thickness plotted at the beginning of the shell acceleration (empty squares) and when the shell has converged by a factor of 2.5 (solid circles).

laser absorption region, significantly reducing the absorption fraction (due to a reduced  $\langle Z^2 \rangle$ ) and, consequently, the ablation pressure.

Since the physics of the ablatively driven implosions is complex, it is important to verify that the key implosion parameters are modeled correctly. The calculated ablation pressure and the mass ablation rate are validated indirectly by comparing the simulated shell trajectory, the power and spectrum of the scattered laser light, and the timing of the neutron production (bang time) with the data. If the ablation pressure in the experiment is reduced compared to the predictions, for example, the observed shell trajectory will be late, resulting in the delayed bang time.

The experimental shell trajectory is inferred from measured spatial profiles of the x-ray emission from the plasma corona obtained using an x-ray framing camera.<sup>19</sup> Figure 4(a) shows a schematic of the coronal emission during shell

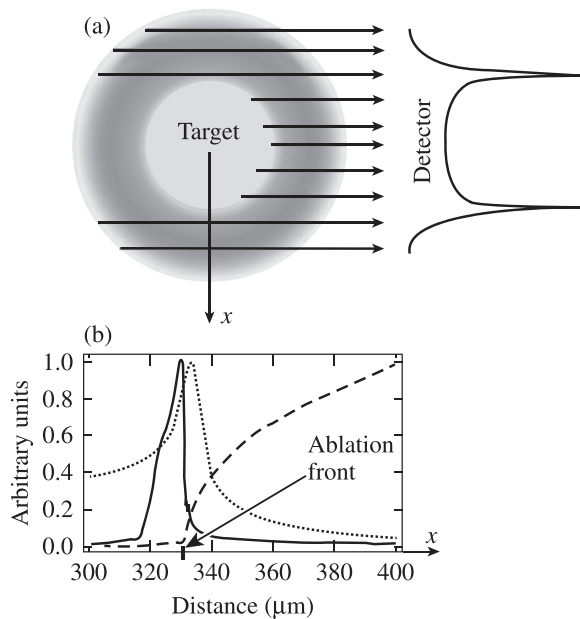


FIG. 4. (a) Sketch of the coronal x-ray emission (left) and a lineout of the self-emission image (right) as measured by an x-ray framing camera. (b) Simulated electron density (solid line), electron temperature (dashed line), and the path-integrated plasma self-emission (dotted line) projected on the detector plane.

acceleration in a direct-drive implosion (darker shades indicate the higher emission) together with a lineout of the self-emission image. Figure 4(b) plots the simulated electron density (solid line), electron temperature (dashed line), and the path-integrated self-emission projected on the detector plane (dotted line) for a typical cryogenic implosion on OMEGA. This figure shows that the ablation front is in very close proximity to the simulated peak in the x-ray emission.

Shell perturbations growing at the ablation front due to the RT instability can potentially shift the position in the peak emission relative to that in the idealized unperturbed implosion because of perturbation spikes that protrude further out into the plasma corona. The nonlinear spike growth, however, is strongly reduced by ablation,<sup>20</sup> limiting spike's amplitude in moderate-adiabat implosions ( $\alpha > 3$ ), as predicted by hydrodynamic simulations, to a few microns (which is comparable to the accuracy in the position measurements,<sup>19</sup> see a discussion later in the text). The effect of perturbation growth on the shape and location of x-ray emission from the plasma corona is illustrated in Figs. 5 and 6. Figure 5 shows snapshots of the simulated mass density maps with (regions II and IV) and without (regions I and III) nonuniformity sources. These snapshots are obtained using the 2-D hydrodynamic code *DRACO*.<sup>21</sup> Laser imprint, target offset, and ice roughness for a typical cryogenic target were used as the nonuniformity sources in the perturbed run. Postprocessing the simulation results using the radiative transfer code *SPECT3D*<sup>22</sup> produces the self-emission profiles plotted in Fig. 6. The emission lineout of the perturbed run (solid line) is obtained by azimuthally averaging the simulated 2-D self-emission image. This lineout is wider and its peak is shifted (mainly due to the low-mode asymmetry) relative to that of the symmetric run (shown with the dashed line), but the position of the steepest emission variation or the “inner edge” of the emission region (marked in Fig. 6 with the thicker vertical line on the left from the peaks) is

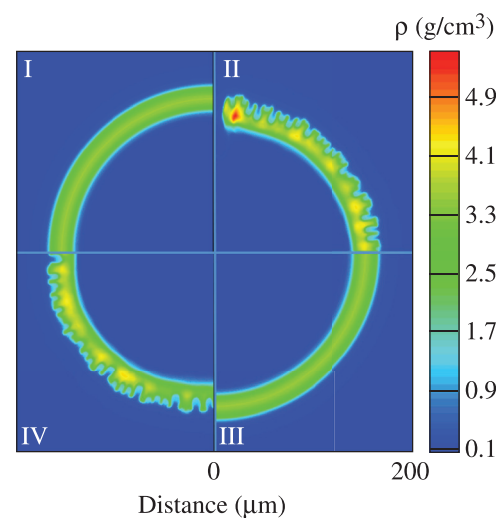


FIG. 5. Simulated shell mass density maps with (regions II and IV) and without (regions I and III) nonuniformity seeds. The snapshots, obtained using the 2-D hydrodynamic code *DRACO*, are taken at the end of the laser drive. The sections in the figure are arranged to emphasize the effect of the low-mode nonuniformity on the ablation-front position (or the outer edge of the higher-density part of the shell).

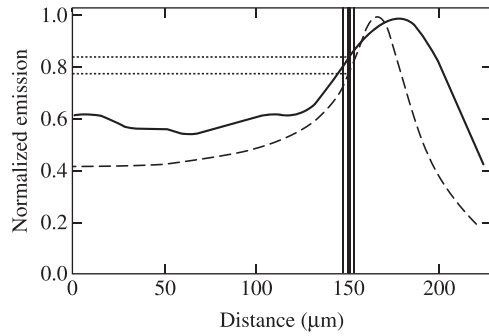


FIG. 6. Comparison of the self-emission profiles obtained using symmetric (dashed line) and perturbed (solid line) *DRACO* simulations. The thick vertical line indicates the position of the inner edge defined in Eq. (6). The thinner vertical lines show the uncertainty in the position measurements. The horizontal dotted lines correspond to the values of  $Em_{\text{edge}}$  [see Eq. (6)] calculated using the results of symmetric (bottom line) and perturbed (top line) *DRACO* runs.

fairly insensitive to the nonuniformity growth in the moderate-adiabat implosions. Because of this, the inner edge position is chosen to compare the simulation results with the data.<sup>23</sup>

Such a comparison is shown in Fig. 7 for an  $\alpha \simeq 4$  cryogenic implosion (shot 72083). The red circles represent the locations of the inner edge  $R_{\text{edge}}$  in the measured self-emission images, and the black squares connected by the solid black line show the inner-edge position obtained using *LILAC* simulations postprocessed with *SPECT3D*. The inner edge in the simulated and measured emission lineouts  $Em$  is defined as a position where

$$Em_{\text{edge}} = 0.65Em_{\text{peak}} + 0.35Em_{\text{min}}. \quad (6)$$

Here,  $Em_{\text{peak}}$  and  $Em_{\text{min}}$  are the peak and the minimum (to the left from the peak) emission values, respectively. To provide a reference, the blue and green dashed lines in Fig. 7 show the calculated ablation-front radius  $R_a$  (defined as the position where the mass density is half of the peak shell

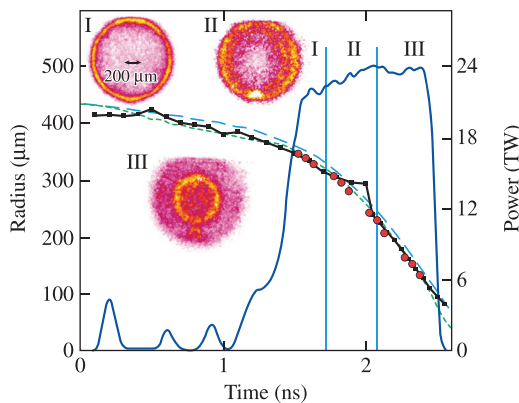


FIG. 7. The predicted ablation-front (blue dashed line) and inner-surface (green dashed line) radii and the measured (red circles) and calculated (black squares connected by the solid black line) locations of the inner edge of the self-emission profiles [calculated using Eq. (6)] for an OMEGA cryogenic implosion (shot 72083). Examples of the self-emission images measured using the x-ray framing camera are shown in the insets numbered by the temporal regions indicated on the main plot. The solid blue line (right axis) shows the measured laser pulse shape.

density at the outer side of the shell) and inner-surface radius  $R_{\text{inner}}$  (the position with the mass density of  $1/e$  of the peak shell density at the inner side of the shell), respectively.

Based on the comparison of the simulated ablation-front and inner-edge positions, the three temporal regions can be identified in Fig. 7: (I)  $t < 1.7$  ns, (II)  $1.7$  ns  $< t < 2.1$  ns, and (III)  $t > 2.1$  ns. The calculated  $R_{\text{edge}}$  (see black line in Fig. 7) follows  $R_a$  and  $R_{\text{inner}}$  in regions I and III and it diverges from them in region II. The deviation in region II occurs because the plastic overcoat is totally ablated from the main shell at  $t \simeq 1.7$  ns and the CD/DT interface starts moving through the ablated plasma region. This forms a double-peak feature in the self-emission profile (see the inset II in Fig. 7 showing an example of the measured emission profile in interval II), affecting the calculated value of  $R_{\text{edge}}$ . To illustrate this effect, Fig. 8 shows the predicted and measured emission profiles at different times during the implosion. Figure 8(a) presents an example of the profile at early times (interval I in Fig. 7) where CD is still being ablated from the main shell. This results in a single peak in the coronal emission (see inset I in Fig. 7) and the well defined inner-edge position. At later times (interval II), when DT is being ablated from the denser part of the shell (the ablation front is in DT), the CD/DT interface is in the ablated-plasma region and located at relatively high electron densities where the emission from CD is comparable to that from the DT near the ablation front [see Fig. 8(b) and inset II in Fig. 7]. In this case, the inner-edge position, as defined by Eq. (6), depends on the relative intensities of the CD and DT peaks in the emission

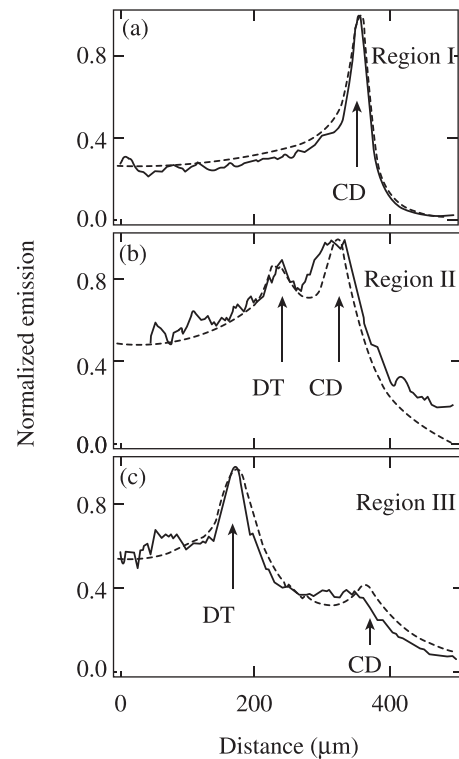


FIG. 8. Lineouts of the self-emission images obtained using *LILAC* simulations postprocessed with *SPECT3D* (dashed lines) and measurements (solid lines) at different times during the  $\alpha \simeq 4$  implosion (shot 72083). Temporal regions I, II, and III are defined in Fig. 7. Positions of the peaks in CD and DT emissions are marked with “CD,” and “DT,” respectively.

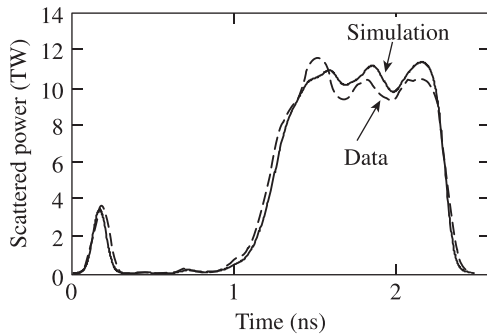


FIG. 9. The measured (dashed line) and predicted (solid line) scattered-light power for the OMEGA cryogenic implosion (shot 69514).

profiles and is affected by the mixing of CD and DT that takes place at the material interface due to hydrodynamic instability growth. This mixing widens the two simulated emission peaks, resulting in broader measured features. When the CD/DT interface moves to the lower-density region (interval III in Fig. 7), emission from CD subsides, making the DT emission dominant and the inner-edge position better defined [see Fig. 8(c) and inset III in Fig. 7].

Taking into account the  $\sim 3\text{-}\mu\text{m}$  accuracy in the measured position of the inner edge in the coronal emission and the  $\sim 20\text{-ps}$  timing accuracy gives the total uncertainty in the measured inner-edge position of  $\sim 8\text{ }\mu\text{m}$  by the end of the laser drive (assuming the maximum ablation-front velocity of  $\sim 360\text{ km/s}$ , which is typical in cryogenic implosions on OMEGA). Then, the accuracy of the ablation pressure calculated using *LILAC* can be estimated by varying the laser-absorption efficiency. Such simulations show that the ablation-front position changes by  $8\text{ }\mu\text{m}$  by the end of the drive pulse if the ablation pressure is varied by  $\sim 13\%$ .

The time-resolved laser absorption and the evolution of the ablated plasma are inferred by measuring the power and spectrum of the scattered light.<sup>24</sup> Figure 9 shows the measured scattered power (dashed line), which agrees very well with predictions (solid line). The measured and predicted total laser absorption fractions are  $55\% \pm 4\%$  and  $55\%$ , respectively.

The measured time-resolved scattered-light spectrum for shot 70802 is compared with a simulation in Fig. 10. The temporal shifts in the scattered laser light are caused by changing optical path length in the plasma traversed by the laser rays. *LILAC* modeling of the scattered light spectrum includes calculating frequency shifts<sup>25</sup> and convolving the results with the incident laser spectrum due to the smoothing by spectral dispersion (SSD).<sup>26</sup> Except for a discrepancy at the beginning of the main drive, both spectra agree very well.

The temporal behavior of the spectrum can be understood by using a simplified description based on a frequency shift of the light reflected from a moving surface (which corresponds to the critical surface where the electron density is equal to  $n_{\text{cr}} \simeq 9 \times 10^{21}\text{ cm}^{-3}$ ). The velocity of the critical surface is plotted in Fig. 11(a). At the early times,  $t < 0.3\text{ ns}$ , this velocity is positive, making the reflecting surface to move toward the observer and causing a blue shift in the spectrum. Later, as the velocity changes to a negative value, the scattered spectrum becomes red-shifted. A sharp feature

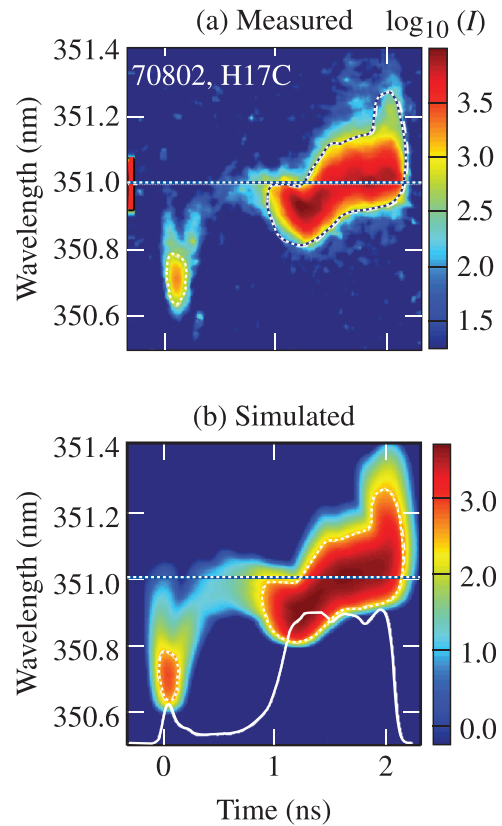


FIG. 10. The measured (a) and predicted (b) scattered-light spectra for the OMEGA cryogenic implosion (shot No. 70802). The white dashed lines mark the 50% simulated intensity contour. They are also shown on the measured spectrum to help the comparison with the data. The pulse shape is shown with the solid white line in (b). The horizontal white dotted line shows incident laser wavelength (zero-shift line) and the red vertical bar at the left axis on (a) indicates the SSD-induced laser bandwidth.

in the spectrum at  $t \simeq 1.3\text{ ns}$  [corresponds to timing marked with the left arrow labeled “red shift” in Fig. 11(a)] is due to the intensity rise and a fast velocity change at the beginning of the main drive. An additional fast velocity variation [see the right arrow labeled “red shift” in Fig. 11(a)] and a sharp red-shifted feature occur at  $t \simeq 1.9\text{ ns}$ . This is due to the onset of the laser deposition in the ablated DT plasma and a mismatch in the electron density across the CD/DT interface, which is a consequence of continuity in pressure (due to momentum conservation) and in the electron and ion temperatures (due to thermal conduction)

$$n_{e,\text{DT}} = n_{e,\text{CD}} \frac{1 + T_i/(Z_{\text{CD}}T_e)}{1 + T_i/(Z_{\text{DT}}T_e)} < n_{e,\text{CD}}, \quad (7)$$

where  $n_{e,\text{CD(DT)}}$  and  $Z_{\text{CD(DT)}}$  are the electron density and the ion charge of the plasma on the CD(DT) side of the CD–DT interface, and  $T_i$  and  $T_e$  are the ion and electron temperatures, respectively. This is illustrated in Fig. 11(b), where the electron density profiles (solid lines) predicted by *LILAC* are plotted at two consecutive times for a typical cryogenic implosion. After the electron density in the expanding CD plasma drops below the critical density at the CD/DT interface, the critical surface position jumps further inward. This is shown in Fig. 11(b) as the critical density (dotted horizontal line) at  $t = t_0$  is inside the CD plasma at  $R \simeq 340\text{ }\mu\text{m}$ . At

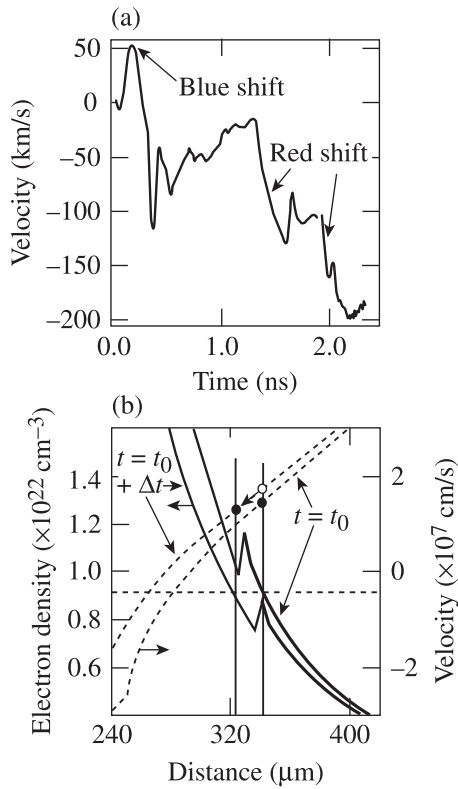


FIG. 11. (a) Simulated velocity of the critical surface. The positive velocity early in the pulse ( $t \approx 0.1$  to  $0.3$  ns) results in a blue shifted part of the scattered light spectrum (see Fig. 10). Fast velocity changes at  $t \approx 1.3$  and  $t \approx 1.9$  ns (shown with two arrows labeled “red shift”) lead to the sharp red-shifted features in the spectrum at the corresponding times. The pulse shape is shown in Fig. 10(b) with the white line. (b) The electron density (solid lines) and flow velocity (dashed lines) in a cryogenic implosion as predicted by *LILAC*. The two vertical lines indicate the positions of the critical electron density (marked with a horizontal dashed line) at two consecutive times during the implosion. The CD/DT interface is localized at the position of discontinuity in the electron density.

$t = t_0 + \Delta t$ , the critical density moves into DT at  $R \approx 324 \mu\text{m}$ . The separation between the two density profiles in the CD region is only  $\sim 5 \mu\text{m}$ . Thus, an additional  $\sim 10\text{-}\mu\text{m}$  shift in the critical-surface position is due to a transition from the CD to DT plasma. As the CD/DT interface travels through the plasma corona region toward the lower electron densities (because of the ablated-plasma expansion),  $T_i$  becomes much smaller than  $T_e$  (the electron-ion energy exchange rate is reduced at lower plasma densities), leading to continuity in the electron density. When the interface is at the critical density, however,  $T_i \approx T_e/2$  and  $n_{e,DT} < n_{e,CD}$ .

The jump in the position of  $n_{cr}$  leads to a reduction in the expansion flow velocity [shown with the dashed lines in Fig. 11(b)] at the critical density. Such a reduction is due to the continuity in the mass flux,  $\rho v$  (where  $\rho = Am_p n_e/Z$ ,  $A$  is atomic mass, and  $m_p$  is proton mass). Without the material change, the velocity at the critical density would change from a value marked by the solid circle at  $t = t_0$  to the open circle at  $t = t_0 + \Delta t$ . With the transition from CD to DT, the flow velocity is reduced to a value marked by the solid circle at  $R = 324 \mu\text{m}$ ,

$$v_{DT}(n_e) = v_{CD}(n_e) \frac{(A/Z)_{CD}}{(A/Z)_{DT}} \approx 0.8 v_{CD}(n_e). \quad (8)$$

The reduction in the expansion velocity at the critical surface makes the critical surface move faster inward, leading to a sharp variation in the critical-surface velocity [see Fig. 11(a)] and the red shifted feature in the scattered-light spectrum at  $t \approx 1.9$  ns. Figure 10 shows that the observed red-shifted part in the spectrum at the end of the pulse is delayed and has a somewhat slower rise than that predicted by *LILAC*. This suggests a smaller CD mass ablation rate in the experiment and a more-gradual transition from CD to DT at the interface, likely due to mixing of CD and DT in the expanding plasma corona.

In summary, the one-dimensional dynamics of cryogenic imploding shells is accurately modeled using *LILAC* by including the nonlocal electron thermal transport<sup>10</sup> and the cross-beam energy transfer<sup>12</sup> models. The 1-D modeling validation is justified in the moderate-adiabat ( $\alpha > 3$ ) implosions where the effect of perturbation growth does not significantly modify laser coupling and shell acceleration history. This result is very important, since the measured target performance degradation relative to the 1-D predictions can be attributed to multidimensional effects, mainly the growth of hydrodynamic instabilities.

### III. TARGET PERFORMANCE

Target performance is quantified by several key observables, including the neutron-averaged areal density, neutron yield, neutron-production history, neutron-average ion temperature, and hot-spot pressure.

#### A. Neutron yield and ion temperature

Figure 12 shows the calculated and measured neutron yields and the neutron-averaged ion temperature as functions of the calculated implosion velocity. The implosion velocity in the simulations is defined as the peak in mass-averaged shell velocity

$$v_{\text{imp}} = \max_{\text{time}}(|v_{\text{shell}}|), \quad v_{\text{shell}} = \frac{\int_{r_1}^{r_2} \rho(r, t) v(r, t) r^2 dr}{\int_{r_1}^{r_2} \rho(r, t) r^2 dr}, \quad (9)$$

where  $r_1$  and  $r_2$  are the positions where the shell density equals  $\rho_{\text{max}}/e$  at the inner and outer sides from the radius of shell peak density, and  $\rho$  and  $v$  are mass density and flow velocity, respectively.

The neutron-averaged ion temperature is calculated using the width of the neutron spectrum  $f_n$ , which includes both thermal and bulk velocity broadening,<sup>27–29</sup>

$$\langle f_n(E) \rangle_V = \frac{\int dV n_1 n_2 \langle \sigma v \rangle_{12} e^{-[\alpha(E) - M_a \cos \theta]^2}}{\int dV n_1 n_2 \langle \sigma v \rangle_{12}}, \quad (10)$$

where  $\alpha(E) = (E - E_0)/\Delta E$ ,

$$\Delta E = 2\sqrt{\frac{m_n T_i E_0}{m_n + m_\alpha}},$$



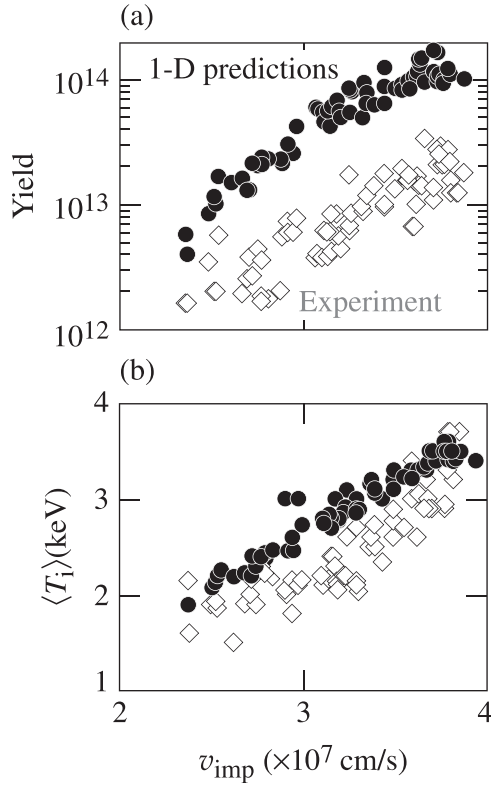


FIG. 12. (a) Measured (open diamonds) and 1-D-predicted (solid circles) neutron yields and (b) the neutron-averaged ion temperature versus calculated implosion velocity for OMEGA cryogenic implosions. The typical error bar for the measured ion temperature is  $\pm 4\%$ .

$\theta$  is the angle between the flow velocity and the neutron detector,  $\langle \sigma v \rangle_{12}$  is the reaction cross section between species 1 and 2,  $n_1$  and  $n_2$  are the ion densities of species 1 and 2, respectively,  $M_a = v/c_s$  is the flow Mach number,  $v$  is the flow velocity,  $c_s = \sqrt{T_i/m_i}$  is the ion sound speed,  $m_i = (m_n + m_\alpha)/2$  is the average ion mass of reaction products,  $E_0 = m_\alpha/(m_n + m_\alpha)Q$ ,  $Q$  is the nuclear energy released in a fusion reaction ( $Q = 17.6$  MeV for D + T reaction), and  $m_n$  and  $m_\alpha$  are the masses of the reaction products (neutron and alpha-particle for DT). Assuming spherical symmetry in Eq. (10) allows evaluation of the integral over angle yielding

$$\langle f_n(E) \rangle_V = \sqrt{\pi} \frac{\int_0^R dr r^2 n_1 n_2 \langle \sigma v \rangle_{12} \text{Er}_-}{4M_a \int_0^R dr r^2 n_1 n_2 \langle \sigma v \rangle_{12}}, \quad (11)$$

where  $\text{Er}_- = \text{erf}[\alpha(E) + M_a] - \text{erf}[\alpha(E) - M_a]$ ,  $\text{erf}(x)$  is the error function, and  $R$  is the size of the neutron-producing region. Integrating Eq. (11) over the neutron-production time and fitting the result with a Gaussian with FWHM =  $\Delta E_{\text{fit}}$ ,

$$\int dt \langle f_n(E) \rangle_V \xrightarrow{\text{fit}} \exp \left[ -4 \ln 2 \left( \frac{E - E_0}{\Delta E_{\text{fit}}} \right)^2 \right],$$

defines an effective temperature

$$\langle T_i \rangle_{n,\text{fit}} = \frac{\Delta E_{\text{fit}}^2}{E_0} \frac{1 + m_\alpha/m_n}{16 \ln 2}, \quad (12)$$

which for DT reactions leads to<sup>29</sup>  $\langle T_i \rangle_{n,\text{fit}} = (\Delta E_{\text{fit}}/177)^2$ . Both  $\Delta E_{\text{fit}}$  and  $T_i$  in the latter equation are in keV. The ion temperature is inferred experimentally by measuring the temporal width of the neutron time of flight,  $\Delta_{\text{TOF}}$ . Using the relation between the neutron energy spread  $\Delta E$  and  $\Delta_{\text{TOF}}$ ,

$$\frac{\Delta E}{E_0} = 2 \frac{\Delta_{\text{TOF}}}{\text{TOF}} \quad \left( \text{where } \text{TOF} = \sqrt{\frac{m_n}{2E_0}} L \right), \quad (13)$$

in Eq. (12) gives

$$\langle T_i \rangle_{n,\text{exp}} = E_0^2 \frac{1 + m_\alpha/m_n}{m_n 2 \ln 2} \left( \frac{\Delta_{\text{TOF}}}{L} \right)^2. \quad (14)$$

For DT, Eq. (14) reduces to

$$\langle T_i \rangle_{n,\text{exp}} = 68 \frac{\Delta_{\text{TOF}}^2}{L^2}, \quad (15)$$

where  $L$  is the distance from detector to target in meters,  $T_i$  is in keV, and  $\Delta_{\text{TOF}}$  is in nanoseconds.<sup>29</sup>

The predicted neutron yield shown in Fig. 12(a) scales as

$$Y_{1D} \sim v_{\text{imp}}^6 \alpha^{-0.8}, \quad (16)$$

while in stark contrast the best fit to the experimental yield gives

$$Y_{\text{exp}} \sim v_{\text{imp}}^{5.0 \pm 0.5} \alpha^{1.0 \pm 0.2}, \quad (17)$$

where  $\alpha$  is defined as the mass-averaged adiabat

$$\alpha = \frac{1}{m_{\text{shk}} - m_b} \int_{m_b}^{m_{\text{shk}}} \frac{p(m)}{\mu \rho(m)^{5/3}} dm, \quad (18)$$

calculated using *LILAC*,  $dm = 4\pi \rho r^2 dr$  is a differential of the mass coordinate,  $m_b$  is the position in the mass coordinate, where  $\rho(m_b) = \rho_{\text{max}}/e$  at the inner shell surface,  $\rho_{\text{max}}$  is the peak density,  $m_{\text{shk}}$  is the shell mass (shocked mass) overtaken by the return shock at the time of the peak neutron production (bang time),

$$\mu = \frac{(3\pi^2)^{2/3} \hbar^2 Z^{5/3}}{5 m_e m_i^{5/3}}, \quad (19)$$

$m_i$  and  $m_e$  are the average ion and electron masses, respectively,  $Z$  is the average ion charge, and  $\hbar$  is the Planck constant. In general,  $\alpha$  increases with time during the shell acceleration, mainly due to radiation heating from the plasma corona. In this paper, the quoted values of adiabat  $\alpha$  are calculated near the beginning of shell acceleration, when  $R_a = 2/3 R_{\text{vapor}} \equiv R_{a,2/3}$ , where  $R_a$  is the ablation-front radius, and  $R_{\text{vapor}}$  is the radius (initial radius) of the vapor region of an undriven shell.

The lower-adiabat implosions are predicted to result in higher fuel compression and higher hot-spot ion temperatures. This leads to an increase in the neutron yields as  $\sim \alpha^{-0.8}$  when multidimensional effects are not taken into

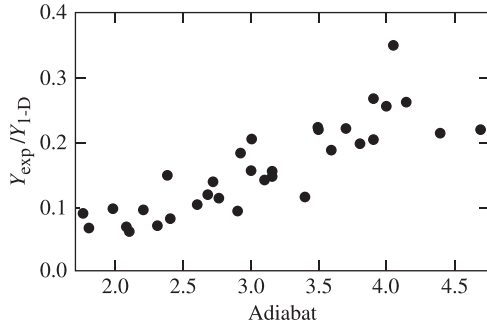


FIG. 13. Experimental yield normalized to *LILAC* predictions. Only data for shells with CD thicknesses of 7.5 to 8.3  $\mu\text{m}$  are shown.

account [see Eq. (16)]. The target performance in an experiment is strongly degraded, however, for the low-adiabat implosions<sup>30</sup> since ablative stabilization is weaker and, consequently, the RT instability growth is larger, leading to a linear dependence of the measured yields on  $\alpha$  [see Eq. (17)]. Figure 13 plots the experimental neutron yields normalized to *LILAC* predictions. As the fuel adiabat gets smaller, the yields drop with respect to the 1-D predictions. This indicates that the shell stability plays a crucial role in determining target performance.

## B. Areal density

Figure 14(a) shows a contour map of the observed areal density averaged over the two independent measurements, using the magnetic recoil spectrometer (MRS)<sup>31</sup> and a highly

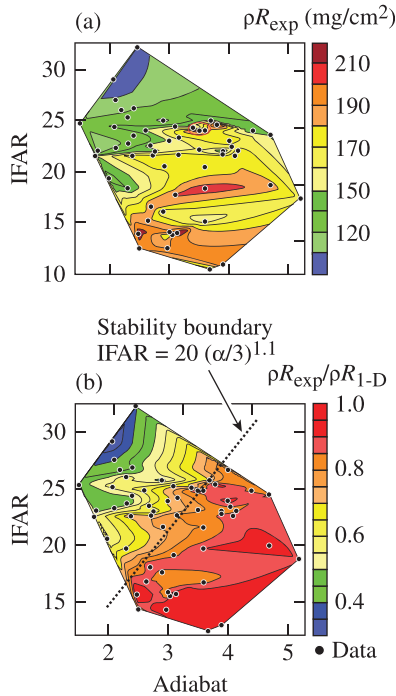


FIG. 14. (a) Contour map of the measured areal density ( $\rho R$ ) as a function of calculated adiabat and IFAR. The contours represent linear fit to the experimental data (black points). (b) Contour map of the measured areal density normalized to *LILAC* predictions. The dashed line (a stability boundary) separates the region where more than  $\sim 85\%$  of the 1-D predictions is observed and the region where the measurements are significantly reduced because of hydrodynamic instability growth. IFAR and adiabat values in the plots are calculated from simulations using Eqs. (18) and (20), respectively.

collimated neutron time-of-flight (nTOF) detector,<sup>32</sup> as a function of calculated adiabat and the target IFAR. Here,

$$\text{IFAR} = \frac{R_{a,2/3}}{\Delta_{2/3}} \quad (20)$$

is defined near the beginning of shell acceleration [see discussion after Eq. (19)]. The shell thickness  $\Delta_{2/3}$  is defined as the distance between the inner and outer positions where the shell density equals the initial density of the ablator ( $\rho = 1.08 \text{ g/cm}^2$  for CD). The black points represent the individual OMEGA shots. The map is created using 2-D linear interpolation of the experimental  $\rho R$  values.

The performance degradation is quantified in Fig. 14(b) where the neutron-average areal density reduction with respect to the 1-D predictions,  $\rho R_{1-D}$ , is plotted in adiabat/IFAR parameter space. As the fuel adiabat gets smaller and the shell IFAR larger, the measured  $\rho R$  drops with respect to the 1-D predictions. Figure 14(b) shows that a stability boundary, defined approximately by

$$\text{IFAR}_{\text{boundary}} \simeq 20(\alpha/3)^{1.1}, \quad (21)$$

separates the region where more than 85% of the 1-D-predicted areal density is observed (on the right side from the boundary) and the region where the measured areal density is significantly reduced because shell compressibility is compromised by nonuniformity growth.

In addition to the hydrodynamic instability growth, preheat caused by suprathermal electrons must be considered as a possible mechanism of the target-performance degradation. The high- and low-adiabat designs are driven at the same peak laser intensities, leading to very similar coronal conditions (such as the electron density and temperature profiles). Thus, the preheat source must be similar for all the designs. Since  $\alpha \sim 4$  implosions achieve  $\sim 90\%$  of the areal densities predicted without the preheat effects and the areal density scales with the fuel adiabat as<sup>34</sup>  $\rho R \sim 1/\sqrt{\alpha}$ , the adiabat increase due to preheat cannot be larger than  $\sim 20\%$  or  $\Delta\alpha_{\text{preheat}} < 0.2 \times 4 = 0.8$ . This modifies the areal-density dependence on the shock-controlled part of the adiabat  $\alpha$  to  $\rho R \sim 1/\sqrt{\alpha + 0.8}$ , which cannot explain the observed areal density degradation in lower-adiabat designs shown in Fig. 14(a). Even though a moderate effect of electron preheat cannot be ruled out, failure to explain the observed  $\rho R$  dependence on adiabat using the preheat argument alone indicates that the preheat is not the dominant performance-degradation mechanism.

## C. Hot-spot pressure

The hot-spot pressure evolution in the experiments is estimated using the ratio of the predicted and measured neutron-production histories. With the help of Eq. (5), the neutron-production rate can be written as

$$\dot{N} \equiv \frac{dN}{dt} \sim p_{\text{hs}}^{7/5} T_i^{2.5}. \quad (22)$$

Then, taking the ratio of the experimental and predicted  $\dot{N}$  the result is used to estimate the experimental hot-spot pressure  $p_{\text{hs}}^{\text{exp}}$ ,

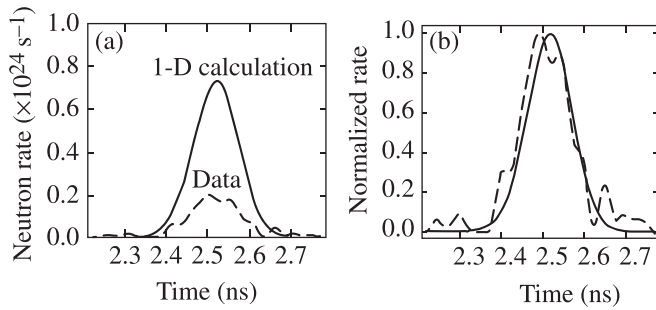


FIG. 15. The measured (dashed lines) and predicted (solid lines) neutron-production histories (a) and normalized neutron rates (b) for an  $\alpha=4$  cryogenic implosion (shot 69514).

$$p_{\text{hs}}^{\text{exp}} \simeq p_{\text{hs}}^{\text{theory}} \left( \frac{T_{\text{exp}}}{T_{\text{theory}}} \right)^{-1.8} \left( \frac{\dot{N}_{\text{exp}}}{\dot{N}_{\text{theory}}} \right)^{0.7}. \quad (23)$$

The neutron-production measurement is time-resolved,<sup>33</sup> while the neutron-averaged ion temperature is a time-integrated quantity. In evaluating Eq. (23), therefore, the time-integrated neutron-averaged temperatures are substituted for both the measured  $T_{\text{exp}}$  and predicted  $T_{\text{theory}}$  ion-temperature histories. Figure 15 shows the temporal evolutions of the measured (dashed lines) and 1-D-predicted (solid lines) neutron-production rates; the predictions include the instrumental as well as the thermal and bulk-velocity broadening, as shown in Eq. (11). The calculated and inferred hot-spot pressures are plotted in Fig. 16 for two OMEGA shots with similar 1-D implosion parameters ( $\alpha \sim 4$ ). The figure indicates that 35% to 40% of the hot-spot pressures predicted by *LILAC* are achieved in moderate-adiabat cryogenic implosions. These inferred pressures are consistent with the results of the hot-spot model described in Ref. 35.

An example of the hot-spot pressure evolution for a lower-adiabat implosion ( $\alpha \sim 2$ ) is shown in Fig. 17. Although the predicted peak pressure increases to 150 Gbar, the pressure inferred in the experiment is reduced compared to that in the higher-adiabat implosions. The hot-spot pressure in the experiment reaches its maximum value ( $\sim 20$  Gbar) early and stays virtually flat during the shell

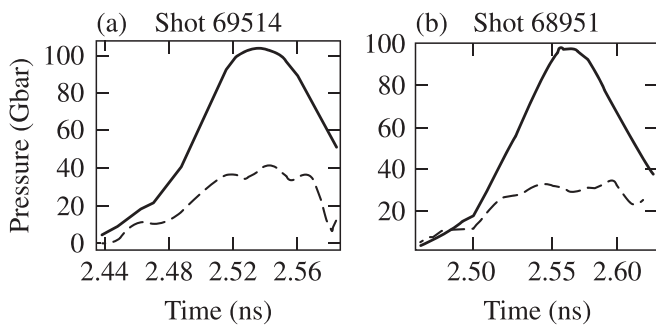


FIG. 16. The calculated (solid lines) hot-spot pressure and the pressure inferred (dashed lines) using the measured neutron-production history and ion temperature for two  $\alpha \simeq 4$  implosions. The predicted and inferred peaks in the central pressure  $p_{\text{max}}$  are 100 Gbar and 41 Gbar (shot 69514) and 100 Gbar and 33 Gbar (shot 68951), respectively. The predicted and inferred neutron-averaged hot-spot pressures  $\langle p \rangle_n$  are 72 Gbar and 29 Gbar (shot 69514) and 66 Gbar and 24 Gbar (shot 68951), respectively.

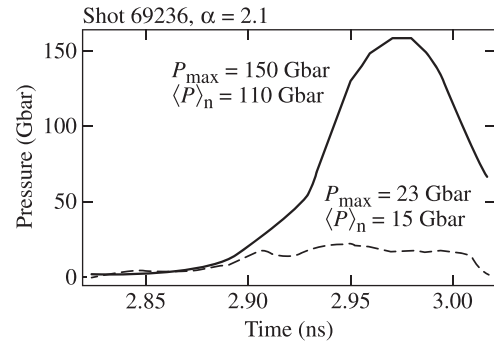


FIG. 17. The predicted (solid line) and inferred (dashed line) hot-spot pressure for an  $\alpha \simeq 2.1$  implosion (shot 69236).

deceleration. This is a result of the hydrodynamic instability growth, which leads to inflight shell breakup and significant cold fuel and ablator material mixing into the hot spot. See Sec. IV B 1 for more discussion.

Two-dimensional maps of the experimental neutron-averaged hot-spot pressures and the ratios of the inferred and predicted pressures are shown in Fig. 18. The hot-spot pressure peaks at  $\alpha \sim 4$  and an IFAR  $\sim 22$ . The pressure is lower in implosions with a smaller IFAR because of the reduced predicted values [lower implosion velocities and higher adiabats lead to lower hot-spot pressures (see Sec. V)]. The reduced pressure for the higher-IFAR implosions is due to a loss in the target stability. This will be discussed in more detail in Sec. IV.

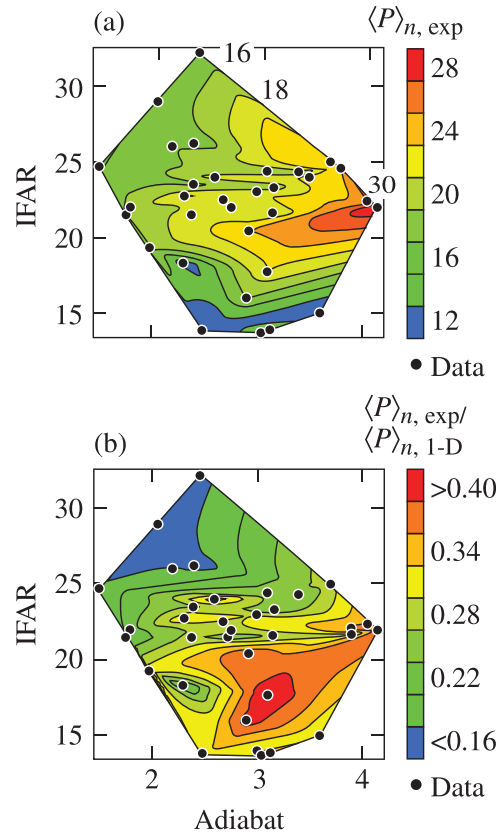


FIG. 18. (a) Contour map of the inferred neutron-averaged hot-spot pressure. The constant-pressure contours with  $\langle p \rangle_n = 16, 18,$  and  $30$  Gbar are labeled on the map. (b) Contour map of the inferred pressure normalized to *LILAC* predictions.

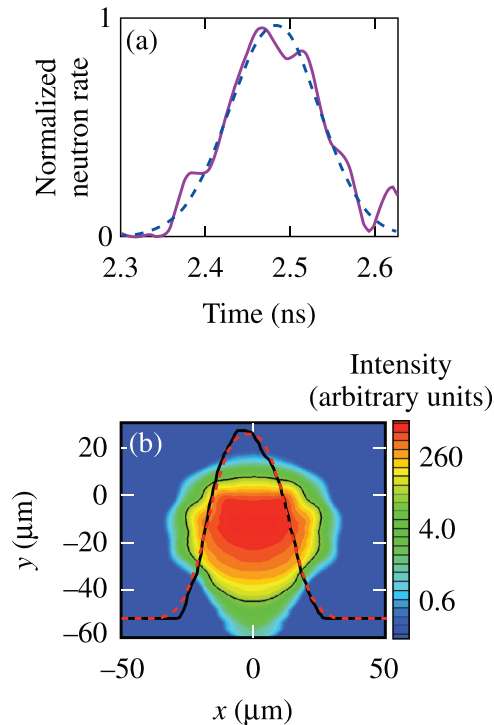


FIG. 19. (a) Normalized neutron-production histories for an  $\alpha=4$  Omega cryogenic shot 69514, measured (solid line) and simulated using the 2-D hydrocode *DRACO* (dashed line). (b) A lineout of the measured time-integrated x-ray emission for the same shot (red dashed line) and the results of a *DRACO* simulation postprocessed using *SPECT3D* [shown as a contour map of intensity and a lineout of this map on a linear scale (black line)].

#### IV. IMPLOSION MODELING

This section describes the analysis of the cryogenic target performance using 2-D hydrodynamic code simulations (Sec. IV A) and simplified analytic models (Sec. IV B).

##### A. Integrated two-dimensional simulations

To improve the target performance and demonstrate the ignition hydrodynamic equivalence of cryogenic implosions on OMEGA, it is important to understand the trends in the experimental data shown in Sec. III. As a first step, the 2-D hydrocode *DRACO*<sup>21</sup> is used to calculate the effects of target surface roughness, short-wavelength, single-beam nonuniformity (laser imprint), and long-wavelength illumination nonuniformities caused by beam power imbalance, the beam overlap pattern, beam mistiming, and target offset. Figure 19 shows simulation results<sup>36</sup> for a mid-adiabat ( $\alpha \sim 4$ ) implosion (OMEGA shot 69514). Table I summarizes predicted and measured performance parameters.  $R_{17}$  in the table refers

TABLE I. Summary of the measured and calculated target performance parameters for an  $\alpha=4$  cryogenic implosion (shot 69514).

Observables	1-D	2-D	Experiment
Yield $\times 10^{13}$	11	3.9	$3.0 \pm 0.1$
$T_i$ (keV)	3.5	3.7	$3.7 \pm 0.3$
$\rho R$ (mg/cm <sup>2</sup> )	209	180	$175 \pm 15$
$p_{hs}$ (Gbar)	83	32	$30 \pm 5$
$R_{17}$ ( $\mu\text{m}$ )	21.7	24.4	$25.2 \pm 0.4$

to the size of the time-integrated x-ray emission region as measured using azimuthally-averaged 17% of the peak emission contour. Table I and Fig. 19 indicate that the neutron yield, areal density, and burn width are in very good agreement with the observables. Figure 19(b) shows that the size of the x-ray image calculated using the *DRACO* simulation post-processed with the radiative transfer code *SPECT3D*<sup>22</sup> is also in good agreement with measurements made using the gated x-ray imager<sup>37</sup> (GMXI).

Simulations of lower adiabat ( $\alpha \sim 2$ ) implosions, however, fail to reproduce the experimental data. The measured areal densities are significantly lower than the simulated values (by a factor of 1.5 to 2), and the experimental burn width and the size of the x-ray emission region are larger as well. The results of simulations are compared with the data in Table II.

This limited ability of the hydrodynamic simulations to explain the observables in the low-adiabat implosions on OMEGA is common to that in indirect-drive cryogenic implosions<sup>38</sup> at the National Ignition Facility (NIF).<sup>39</sup> To understand the factors limiting the target performance, it is not sufficient to rely solely on the simulations because of uncertainties in the physical models used in these codes. In addition, not all the sources of the target and illumination nonuniformities can be identified and characterized with the precision required to resolve the performance-relevant spatial scales. Simplified theoretical models can help in developing physical understanding of the implosion dynamics and failure mechanisms. Such models will be described next.

##### B. Simplified models of the implosion dynamics

The peak hot-spot pressure can be estimated using the argument that stopping the incoming shell (fuel) material with density  $\rho_{shell}$  and velocity  $v_{imp}$  by a strong shock requires the shock pressure of

$$p_{max} \simeq 4/3 \rho_{shell} v_{imp}^2. \quad (24)$$

Using the in-flight shell quantities (an ablation pressure of 100 Mbar, fuel adiabat  $\alpha \sim 1$ , and shell velocity  $v_{imp} = 4 \times 10^7$  cm/s), Eq. (24) gives only  $p_{max} \simeq 4/3(p_a/2.2\alpha)^{3/5} v_{imp}^2 = 4/3(100 \text{ Mbar}/2.2)^{3/5} (4 \times 10^7)^2 = 21$  Gbar, an order of magnitude lower than the peak pressure predicted in a hydrodynamic code simulation at these conditions. The source of the pressure deficiency in using this simple argument is the spherical convergence effects, which are important during the final stages of the hot-spot formation. The shell convergence increases the

TABLE II. Summary of measured and calculated target performance parameters for an  $\alpha=2$  cryogenic implosion (shot 69236).

Observables	1-D	2-D	Experiment
Yield $\times 10^{13}$	18	1.7	$1.1 \pm 0.1$
$T_i$ (keV)	3.6	2.9	$2.8 \pm 0.2$
$\rho R$ (mg/cm <sup>2</sup> )	270	190	$112 \pm 13$
Burn width (ps)	52	80	$115 \pm 10$
$p_{hs}$ (Gbar)	110	41	$18 \pm 5$
$R_{17}$ ( $\mu\text{m}$ )	20.2	22.1	$33.3 \pm 0.4$



density of the incoming shell during the deceleration ( $\rho_{\text{shell}} \gg \rho_{\text{inflight}}$ ). In addition, the negative pressure gradient inside the shock-compressed part of the shell (see Fig. 1(b)) increases the hot-spot pressure relative to the shock pressure estimated using Eq. (24) by a factor of 2 to 3. Because peak stagnation pressures exceeding 100 Gbar are required in an igniting hot spot, it is crucial to understand the dynamics of shell deceleration and the hot-spot pressure amplification near stagnation.

The hot-spot pressure dependence on the shell convergence provides a starting point in describing the deceleration dynamics. Since the thermal conduction losses from the hotter central region to the colder shell material are balanced by the internal energy flux of the ablated material back into the hot spot, the pressure inside the hot spot is not affected by the ablation and can be calculated using the adiabatic approximation,<sup>3</sup>  $p_{\text{hs}} \sim V_{\text{hs}}^{-5/3}$ , where  $V_{\text{hs}}$  is the hot-spot volume. If  $V_{\text{hs0}}$  and  $p_{\text{hs0}}$  are the volume and pressure of the vapor region at the beginning of shell deceleration, then the time evolution of the hot-spot pressure is described by

$$p_{\text{hs}} = p_{\text{hs0}} \left( \frac{V_{\text{hs0}}}{V_{\text{hs}}} \right)^{5/3}. \quad (25)$$

As the hot spot approaches stagnation and the electron temperature starts to rise (the electron–ion energy exchange rate increases with the hot-spot density), the hot-spot mass increases because of mass ablation from the inner part of the shell. Consequently, the temporal behavior of the central pressure cannot be described by the central density alone,  $p_{\text{hs}} \not\sim \rho_{\text{hs}}^{5/3}$ , even though Eq. (25) is satisfied. The central pressure peaks as the hot-spot volume reaches its minimum value  $V_{\text{min}}$ ,

$$p_{\text{max}} = p_{\text{hs0}} \left( \frac{V_{\text{hs0}}}{V_{\text{min}}} \right)^{5/3}. \quad (26)$$

Calculating the peak central pressure, therefore, reduces to determining the vapor pressure  $p_{\text{hs0}}$  at the beginning of shell deceleration and the hot-spot volume reduction fraction during deceleration  $V_{\text{hs0}}/V_{\text{min}}$  (this is related to the hot-spot convergence ratio  $\text{Cr}$ ,  $p_{\text{max}} \sim \text{Cr}^5$ , in a 1-D implosion).

The shell position and the vapor volume  $V_{\text{hs0}}$  at the start of deceleration are the key parameters since the farther the shell moves inward before it begins to decelerate, the higher the shell density  $\rho_{\text{shell}}$  (because of the convergence effects) and, according to Eq. (24), the higher the maximum pressure ( $\rho_{\text{shell}} v_{\text{imp}}^2$  is larger because of the higher  $\rho_{\text{shell}}$ ). The shell deceleration begins when the vapor pressure, amplified by the shell convergence, exceeds the shell pressure (which increases with the ablation pressures). Onset of shell deceleration, therefore, depends on the evolution of the vapor and shell pressures during the shell acceleration. The factors determining the vapor pressure history will be discussed next.

### 1. Vapor pressure evolution

Three main effects contribute to the increase in vapor pressure during the implosion: (1) the compression of the initial vapor mass introduced into the central part of the target during the cryogenic-layer formation; (2) the density

rarefaction (material release) at the inner part of the shell during the acceleration; and (3) excessive nonuniformity growth that leads to shell breakup, injecting the colder shell and hotter plasma-corona materials into the vapor region.

The first contribution can be calculated using the pressure–density relation

$$p_{v,1} = \mu \alpha_v \rho_v^{5/3}, \quad (27)$$

where  $\alpha_v$  is adiabat of the vapor region,  $p_{v,1}$  and  $\rho_v$  are the vapor pressure and density, and  $\mu$  is defined in Eq. (19). As the vapor volume  $V_v$  gets smaller during the shell convergence, the average vapor density increases as

$$\rho_v = \rho_{v0} V_{v0}/V_v, \quad (28)$$

where  $\rho_{v0}$  and  $V_{v0}$  are density and volume of the vapor region in an undriven target. Neglecting ion kinetic effects [see discussion after Eq. (32)], the vapor adiabat is determined mainly by shock heating

$$\alpha_v = \frac{p_{v,\text{shk}}}{\mu \rho_{v,\text{shk}}^{5/3}}, \quad (29)$$

where  $p_{v,\text{shk}}$  and  $\rho_{v,\text{shk}}$  are pressure and density behind the leading shock that travels in the vapor ahead of the shell. Since the leading shock is strong,  $\rho_{v,\text{shk}} \simeq 4\rho_{v0}$ . It can be shown that the relation between the ablation and shock pressures takes the form

$$p_{v,\text{shk}} \simeq p_{a0} \frac{\rho_{v0}}{\rho_0} \left\{ 1 + 2\sqrt{5} \left[ 1 - \left( \frac{\rho_{v0}}{\rho_0} \right)^{1/5} \right] \right\}, \quad (30)$$

where  $p_{a0}$  is the ablation pressure at the beginning of shell acceleration and  $\rho_0$  is the initial (undriven) main fuel density ( $\rho_0 \simeq 0.25 \text{ g/cm}^3$  for DT ice). Using Eqs. (27)–(30) gives the vapor adiabat

$$\alpha_v = \frac{p_{a0}}{\mu \rho_{v0}^{5/3}} F \left( \frac{\rho_{v0}}{\rho_0} \right), \quad (31)$$

where

$$F(x) = \frac{x}{4^{5/3}} [1 + 2\sqrt{5}(1 - x^{1/5})],$$

and the contribution to the vapor pressure increase caused by the convergence of the initial vapor mass becomes

$$p_{v,1} \simeq p_{a0} F \left( \frac{\rho_{v0}}{\rho_0} \right) \left( \frac{V_{v0}}{V_v} \right)^{5/3}. \quad (32)$$

The convergence effects of the leading shock wave break the validity of Eq. (30) near the target center and Guderley's solution<sup>40</sup> must be used. The volume of the vapor region where this occurs, however, is small compared to the total vapor volume. A correction to the vapor pressure caused by an increase in the shock strength near the origin, therefore, is small.

Strictly speaking, the shock convergence effects near the target center cannot be described using Guderley's

solution either because of ion heating, which becomes strong enough to raise the ion temperature to a few keV at the shock front. The ions in the high-energy tail of the distribution function in this case travel ahead of the shock position defined using the hydrodynamic approximation.<sup>41</sup> This preheats the vapor region, raising its adiabat and pressure.

Equation (32) shows that the vapor pressure decreases when the initial vapor density  $\rho_{v0}$  is reduced. Therefore, minimizing the initial vapor mass improves the areal densities at peak compression by increasing the shell convergence prior to the onset of the deceleration.

The lower limit of the vapor pressure (when the initial vapor mass is very small) is determined by the density rarefaction formed at the inner part of the shell during the implosion. A low-density tail of the released material travels inward ahead of the higher-density part of the shell, contributing to the vapor mass and pressure. A simplified scaling for the contribution of the released material to the vapor mass can be obtained by assuming that a strong shock with a pressure  $p_a$  breaks out of a material with the post-shock sound speed  $c_{sa}$  and density  $\rho_a$  into the material with density  $\rho_{v0}$ . The released material (rarefaction tail) moves inward in this approximation with the velocity<sup>42</sup>

$$v_{\text{tail}} = v_{\text{shell}} + 3c_{sa} \left[ 1 - \left( \frac{p_{v,\text{shk}}}{p_a} \right)^{1/5} \right], \quad (33)$$

where  $p_{v,\text{shk}}$  is calculated using Eq. (30). The accumulated mass in the rarefaction tail calculated from the lowest-density point up to the density  $\rho$  is

$$m_{\text{rf}}(\rho) \simeq 4\pi R^2 c_{sa} \rho_a t C_\rho, \quad (34)$$

where

$$C_\rho = \left( \frac{\rho}{\rho_a} \right)^{4/3} - \left( \frac{p_{v,\text{shk}}}{p_a} \right)^{4/5},$$

$R$  is shell position, and  $t$  is the shell acceleration time. Since the tail moves inward with a velocity greater than the shell velocity [see Eq. (33)], the accumulated mass in the rarefaction increases with time, as shown in Eq. (34). Substituting the total shell acceleration time  $t = t_{\text{imp}} \sim E_L / (4\pi R^2 I)$  (where  $E_L$  is the laser energy and  $I$  is the laser intensity) into Eq. (34) and writing the mass density as  $\rho_a \sim (p_a / \alpha_{\text{inner}})^{3/5}$  gives the scaling for the mass in the rarefaction tail at the end of the shell acceleration,

$$m_{\text{rf}} \sim \left( \frac{E_L}{I} \right) \alpha_{\text{inner}}^{-3/10} p_a^{4/5} C_\rho, \quad (35)$$

where  $\alpha_{\text{inner}}$  is the adiabat of the released material (inner part of the shell). Then, the contribution to the vapor pressure caused by the mass buildup due to the rarefaction tail (the second contribution to the vapor pressure in our notation),

$$p_{v,2} = \mu \alpha_{\text{inner}} \left( \frac{m_{\text{rf}}}{V_v} \right)^{5/3}, \quad (36)$$

with the help of Eq. (35) and the scaling for the initial radius of the vapor region [see Eq. (74) below] becomes

$$p_{v,2} \sim C_\rho^{5/3} \sqrt{\alpha_{\text{inner}}} \frac{p_a^{4/3}}{v_{\text{imp}}^{5/3}} \left( \frac{V_{v0}}{V_v} \right)^{5/3}. \quad (37)$$

Matching Eq. (37) with the simulation results leads to using  $\rho/\rho_a \sim 0.1$  in the coefficient  $C_\rho$ . As the initial vapor density  $\rho_{v0}$  increases,  $p_{v,\text{shk}}/p_a$  increases as well (reducing  $C_\rho$ ) and the contribution to the hot-spot pressure from the material released into the target center becomes small. Equation (37) tends to overestimate the pressure because Eqs. (33) and (34) are written in the shell frame of reference, assuming that  $v_{\text{shell}}$  is a constant in time. The shell velocity in ICF implosions, however, increases with time, reducing the velocity difference between the shell and the trailing edge of the rarefaction wave. This makes the mass in the rarefaction tail smaller than predicted by Eq. (35).

Since the contribution to the vapor pressure due to the rarefaction depends on the adiabat  $\alpha_{\text{inner}}$ , material heating at the inner part of the shell caused by shock mistiming, radiation, or suprathermal electrons can result in a greater material expansion and a significant reduction in the peak of the hot-spot pressure compared with the case when such heating is not taken into account. In an optimized design, the gain in the vapor mass caused by the material release during the acceleration is minimized by accurately timing shocks emerging from the cold fuel shell.

The third contribution to the pressure and the mass enhancement in the vapor region during acceleration is due to multidimensional effects. These include jets of material created by local shell nonuniformities as well as fluxes of ablated plasma through the holes in the shell that result from excessive RT growth at the ablation front. These effects lead to an injection of material with relatively high adiabat  $\alpha_{\text{mix}} \gg \alpha_{\text{shell}}$  (see Ref. 43). The vapor pressure contribution caused by the mix is

$$p_{v,3} = \mu \alpha_{\text{mix}} \left( \frac{m_{\text{mix}}}{V_v} \right)^{5/3}, \quad (38)$$

where  $m_{\text{mix}}$  is the injected mix mass and  $\mu$  is defined in Eq. (19).

The effect of shell breakup and ablator mass injection into the vapor region was studied in Ref. 43, where a series of 2-D *DRACO* simulations was performed assuming a distribution of localized mass perturbations of 5 to 30  $\mu\text{m}$  in diameter and 0.5 to 1  $\mu\text{m}$  in height as an initial nonuniformity source on the outside of the target. The simulations show that these features distort the first shocks launched by the intensity pickets early in the laser pulse, introducing significant modulations in the lateral mass flow and creating low-density bubbles inside the ablator and the main fuel layer at the beginning of shell acceleration. Since there is no stabilizing effect of the ablation inside the cold bubbles,<sup>44</sup> the bubble growth gets enhanced as the shell starts to accelerate. The bubble velocity<sup>45</sup>  $v_{\text{bubble}} \sim \sqrt{d_{\text{bubble}} g}$  (where  $d_{\text{bubble}}$  is the bubble diameter and  $g$  is the shell acceleration) competes with the material release rate at the inner surface of the shell [see Eq. (35)] and shell thickening due to convergence.

When the bubble amplitude exceeds the in-flight shell thickness, the bubble “bursts” into the vapor region, injecting the ablator and the cold fuel mass into the central part of the target. In addition, the pressure difference between the ablation front and the vapor region creates a flow of ablated material from the plasma corona into the vapor region. Since the material releases slower [see Eq. (35)] and the shells get thinner with a reduction in the adiabat, the lower-adiabat target designs are more susceptible to the shell break up because of bubble growth.

The simulation results, summarized in Fig. 9 of Ref. 43, indicate that to reduce the peak areal density by a factor of 2, the ablator and cold fuel material must be injected with a mass larger than  $\sim 15\times$  the initial vapor mass. For DT vapor at the triple point, the initial mass density is  $\sim 0.6\text{ mg/cm}^3$ , which corresponds to the initial vapor mass of  $0.12\text{ }\mu\text{g}$  and the injected mix mass of  $\sim 2\text{ }\mu\text{g}$  required to explain the observables in the low-adiabat implosions.

Next, the inferred hot-spot pressure and the measured neutron-production rate in an  $\alpha \sim 2$  cryogenic implosion are compared with the results of *DRACO* simulations in Fig. 20. The level of the preimposed local defects in these simulations was varied to match the observed neutron-averaged areal density and neutron yield. This leads to approximately  $2\text{ }\mu\text{g}$  of ablator and main fuel material being injected into the vapor region because of hydrodynamic instability growth, as calculated in these simulations. Even though the predicted neutron-averaged areal density is being forced to match the

data, the close comparison of the temporal behavior of the observables with simulation results shown in Fig. 20 gives an additional validation of the mix hypothesis. The excellent agreement between simulation results and the data suggests that, indeed, the degradation in the performance of the low-adiabat implosions results from a significant mixing of the ablator material into the vapor region.

The main source of the localized nonuniformities in OMEGA cryogenic targets, however, remains unknown. Significant shock distortions can be caused by either surface features or ice defects localized at the CD/DT interface created, for example, as a result of early-time laser shinedthrough.<sup>46</sup>

In summary, the pressure build up inside the accelerating target is caused by compression of the original vapor mass, material release from the inner part of the shell, and mixing of the ablator and cold fuel inside the target vapor region in the designs with excessive RT growth at the ablation front. Higher central pressure during acceleration causes an early shell deceleration and stagnation, resulting in lower final fuel compression.

## 2. Shell acceleration and shell pressure evolution

The onset of the shell deceleration depends not only on the vapor pressure but also on the shell pressure because the shell begins to slow down when the former exceeds the latter, creating the radial pressure gradient pointing toward the target center.

During the early stages of an implosion, when convergence effects are not important, the maximum shell pressure is equal to the ablation pressure and the pressure peak is localized near the ablation front. When convergence becomes important, the pressure maximum exceeds the ablation pressure and its location moves inside the shell.

The basic features of the shell dynamics in convergent geometry can be studied using a model based on an approximate solution of the momentum-conservation equation. In this model (described in details in Appendix A), the shell pressure is written as a second-order polynomial in the mass coordinate

$$p(m, t) = p_a[1 + \hat{p}_1(t)(1 - m/M) + \hat{p}_2(t)(1 - m/M)^2], \quad (39)$$

where  $m$  is the mass coordinate defined by the differential equation  $dm/dr = 4\pi\rho r^2$ ,  $M$  is the shell mass,  $r$  is position, and  $\rho$  is the shell density. The maximum shell pressure  $p_{\text{shell}}$  equals the ablation pressure  $p_a$  when  $\hat{p}_1 < 0$ ;  $p_{\text{shell}}$  exceeds  $p_a$  when  $\hat{p}_1$  becomes positive because of convergence effects [see Eqs. (A11) and (A13) for the dependence of  $\hat{p}_1$  on the implosion parameters]. In the latter case, the peak pressure moves inside the shell and, consequently, the ablation front stops accelerating [see Eq. (A9)]. The time at which the pressure gradient at the ablation front changes from a positive to a negative value plays an important role in the target design because this is when the absorbed laser energy stops contributing to the shell acceleration. Thus, in an optimized implosion, the end of the laser drive must occur when

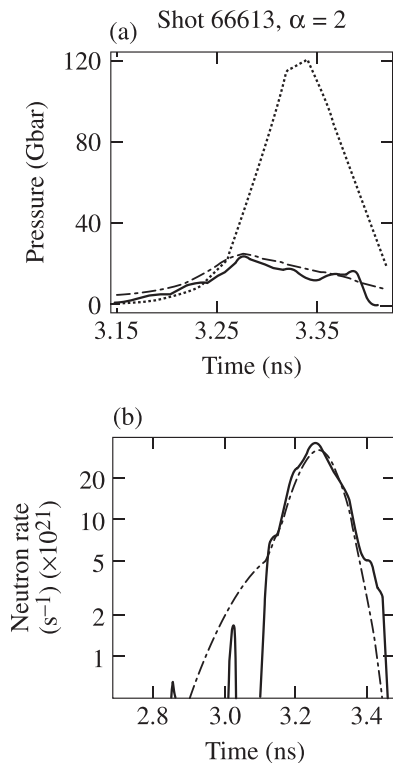


FIG. 20. (a) The hot-spot pressure evolutions inferred from the measurements (shot No. 66613) using Eq. (23) (solid line) and predicted by *LILAC* (dotted line) and *DRACO* (dashed-dotted line). (b) The neutron production histories measured (solid line) and predicted (dashed-dotted line) using *DRACO* simulations with preimposed local defects on the outer surface of the target.

$\hat{p}_1 \simeq 0$ , as the laser energy deposited in the plasma corona after this time does not contribute to kinetic energy of the main shell.

The ablation-front position at this time can be calculated with the help of Eqs. (A11) and (A13),

$$\frac{R_a}{R_0} \simeq \left[ \epsilon \frac{M \dot{R}_a^2 / 2}{4\pi R_0^3 p_{a0}} (2 - 3\beta/5)(1 - \beta/5) \right]^{1/(6-8/5\beta)}, \quad (40)$$

where  $R_a$  is the ablation-front radius and  $p_{a0}$  and  $R_0$  are the ablation pressure and ablation-front radius at the beginning of the shell acceleration. The power index of the ablation-pressure evolution  $\beta$  and the parameter  $\epsilon$  are defined in Eqs. (A5) and (A7), respectively. Equation (40) can be rewritten as

$$\frac{M}{\rho_a V_a} \times \frac{M \dot{R}_a^2 / 2}{(3/2)p_a V_a} = \frac{1}{(1 - 3\beta/10)(1 - \beta/5)} \sim 1, \quad (41)$$

where  $V_a = (4\pi/3)R_a^3$  is the target volume, and  $\rho_a$  is the shell density at the ablation front (which equals the peak shell density in a typical design). The first term in the left-hand side of Eq. (41) is proportional to the ratio of the shell thickness to the ablation-front radius (this ratio is inversely proportional to the IFAR). The second term is the ratio of the shell kinetic energy  $E_k$  and the internal energy  $E_{in,a} = (3/2)p_a V_a$ . The IFAR decays and the ratio of energies increases as the shell converges and accelerates. Thus, the ablation front stops accelerating when IFAR reduces to

$$\text{IFAR} \sim \frac{E_k}{E_{in,a}}. \quad (42)$$

The shell kinetic energy and the ablation pressure do not depend on the shell adiabat, and, for given shell radius and the ablation pressure, the IFAR is larger when the shell adiabat is lower (IFAR  $\sim \alpha^{-3/5}$ ). Consequently, according to Eq. (42), compared with the higher-adiabat case, the lower-adiabat shells accelerate for longer distances [similar conclusion can be reached if Eq. (40) is evaluated replacing  $M \dot{R}_a^2 / 2$  with the shell kinetic energy shown in Eq. (A15)]. Although the higher ablation-front convergence ratios in the lower-adiabat implosions lead to higher 1-D shell densities and hot-spot pressures during deceleration, the RT growth factors at the ablation front are higher, making the lower-adiabat shells more susceptible to nonuniformity growth.

The condition for the end of the ablation-front acceleration, Eq. (41), can also be written in terms of the ablation-front Mach number,  $|\dot{R}_a|/c_s$ ,

$$\rho_a V_a = M \frac{|\dot{R}_a|}{c_s} \sqrt{\left(\frac{1}{3} - \frac{\beta}{10}\right) \left(\frac{5}{3} - \frac{\beta}{3}\right)}, \quad (43)$$

where  $c_s = \sqrt{(5/3)(p_a/\rho_a)}$  is the shell sound speed. The numerical factor in Eq. (43) varies from 0.45 to 0.65 for values of  $\beta$  relevant to ICF implosions. During the implosion, the shell density times the target volume,  $\rho_a V_a$ , decreases (mainly because of a reduction in volume), and the shell

Mach number increases (because of an increase in  $|\dot{R}_a|$ ). Then, Eq. (43) shows that the ablation pressure stops accelerating the ablation front when these two terms are equal,  $\rho_a V_a \sim M |\dot{R}_a| / c_s$ .

Even though the ablation-front velocity does not increase after Eqs. (40)–(43) are satisfied, the inner parts of the shell where the pressure gradient is positive are still being accelerated [see, for example, the pressure and density profiles inside the shell in Fig. 1(a); the shell is being accelerated inside the region  $60 \mu\text{m} < r < 82 \mu\text{m}$  and decelerated where  $r > 82 \mu\text{m}$ ]. The total shell kinetic energy, therefore, keeps increasing until the vapor pressure exceeds the shell pressure and a return shock is launched into the incoming shell.

In addition to determining the duration of efficient laser energy coupling to shell kinetic energy, the onset of the ablation-front deceleration also controls the unshocked-shell density evolution during deceleration (here, “unshocked” means relative to the return shock from the origin as indicated in Fig. 1). Indeed, the sooner the ablation front stops accelerating, the longer the negative pressure gradient decelerates the ablation-front region prior to the return shock formation, and the larger the velocity gradient in the shell. This leads to a reduced shell density and, consequently, lower stagnation pressure [see Eq. (24) and the discussion in Sec. IV B 3]. Thus, delaying the onset of the ablation-front deceleration is beneficial for maximizing the 1-D peak hot-spot pressure. If multidimensional effects are taken into account, however, the longer acceleration distances lead to enhanced RT growth factors at the ablation front.

As discussed in Sec. II, the ablation-front trajectory and onset of the ablation-front deceleration can be inferred experimentally by imaging the x-ray emission from the plasma corona. This is a crucial measurement facilitating target design optimization.

After the location of the peak pressure moves from the ablation front to inside the shell (because of convergence effects), the shell mass coordinate of this location and the value of the peak pressure become

$$m_p = M \left( 1 - \frac{1 + \hat{p}_2}{2\hat{p}_2} \right), \quad (44)$$

$$p_{\text{shell}} = -p_a \frac{(1 - \hat{p}_2)^2}{4\hat{p}_2}, \quad (45)$$

respectively. Note that  $p_{\text{shell}}$  is positive because  $\hat{p}_2$  is negative. At this stage in the implosion,  $\hat{p}_2$  [shown in Eq. (A13)] can be simplified to

$$\hat{p}_2 \simeq -\frac{M \dot{R}_a^2 / 2}{3/2 p_a V_a} \frac{C_\beta}{1 + 6/(4 - 3/5\beta) \rho_a V_a / M}, \quad (46)$$

where the coefficient  $C_\beta = (2 - 3/5\beta)(3 - 3/5\beta)/(4 - 3/5\beta) \simeq 1$  ranges between 0.8 and 1.2 for the values of  $\beta$  relevant to the direct-drive implosions.

In summary, the start of the shell deceleration is determined by the relative evolutions of the vapor [Eqs. (32), (37), and (38)] and the shell [Eq. (45)] pressures. The 1-D target performance increases when the onset of deceleration



is delayed. This is achieved by maximizing the shell and ablation pressures and minimizing the vapor pressure. The ablation front stops accelerating when  $|\dot{R}_a|/c_s \sim \rho_a V_a/M$ . The early ablation-front deceleration in shells with higher adiabats, larger masses, and lower ablation-front densities leads to larger velocity gradients inside the main shell and lower shell densities during deceleration, resulting in reduced stagnation pressures.

### 3. Shell deceleration

Soon after the vapor pressure exceeds the shell pressure [see Fig. 1(a)], a shock is formed at the inner surface of the shell, as illustrated in Fig. 21. The shock travels from the vapor region toward the ablation front. The inner part of the shell overtaken by the return shock (the shocked shell, region II in Fig. 22) is being decelerated by a force that is a consequence of the higher pressure at the hot spot,  $p_{hs}$ , and the lower pressure at the shock front,  $p_{shock}$ . The hot-spot pressure continues to increase, according to Eq. (25), while the shocked shell converges inward and the hot-spot volume decreases (if multidimensional effects are taken into account, the volume history depends also on the hot-spot distortion growth).

The model describing the evolution of the shell and hot spot during shell deceleration is presented in Appendix B. Here, the main results are summarized.

The evolution of the hot-spot radius  $R_{hs}$  is determined by the momentum-conservation equation (Newton's law),

$$\ddot{R}_{hs} = S_{hs} \frac{p_{hs} - p_{shock}}{M_s} \left( 1 - \frac{M_s}{6\rho_{shock0} V_{hs0}} \right)^{-1}, \quad (47)$$

where  $S_{hs}$  is the surface area of the hot spot,  $\rho_{shock0}$  and  $V_{hs0}$  are the shell density at the inner edge of the shell and the hot-spot volume at the beginning of shell deceleration, respectively (see Fig. 21), and  $M_s$  is the mass of the shocked shell (shocked mass). The factor inside the brackets in Eq. (47) is due to the nonlinear dependence of the pressure inside the shocked shell (region II in Fig. 22) on the mass coordinate. The shocked mass, shock pressure, and shock position are determined by Hugoniot conditions,<sup>42</sup>

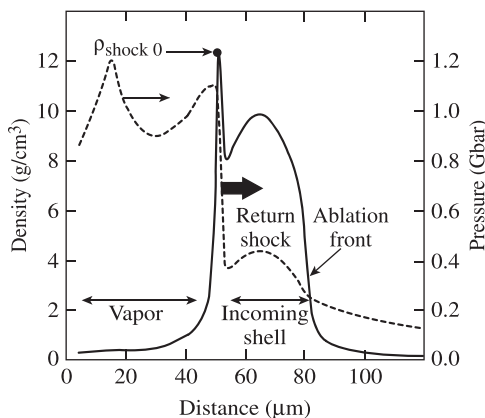


FIG. 21. The density (solid line, left axis) and pressure (dashed line, right axis) profiles at the time when the return shock is launched into the incoming shell.

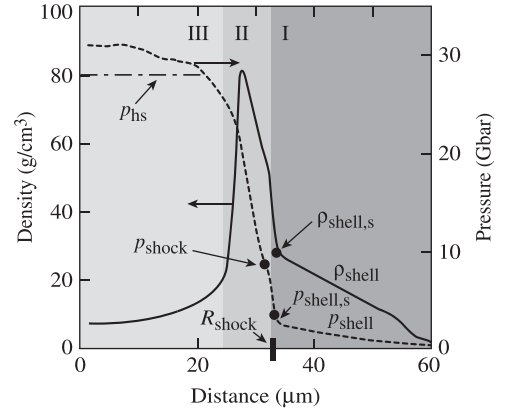


FIG. 22. Snapshots of the density (solid line, left axis) and pressure (dashed line, right axis) profiles during shell deceleration. The following three regions can be identified at this time: (I) the unshocked shell, (II) the shocked shell, and (III) the vapor region (hot spot).

$$\frac{dM_s}{dt} = \sqrt{\frac{\rho_{shell,s}}{3}} \sqrt{4p_{shock} + p_{shell,s}} S_{shock}, \quad (48)$$

$p_{shock}$

$$= p_{shell,s} - \sqrt{\frac{\rho_{shell,s}}{3}} (4p_{shock,s} + p_{shell,s}) (v_{shell,s} - v_{shock}), \quad (49)$$

and

$$\frac{dR_{shock}}{dt} = \sqrt{\frac{4p_{shock} + p_{shell,s}}{3\rho_{shell,s}}} + v_{shell,s}, \quad (50)$$

where  $S_{shock}$  is the shock-front area. Refer to Fig. 22 for definitions of  $\rho_{shell,s}$ ,  $p_{shell,s}$ , and  $p_{shock}$ . Velocity in region (I)  $v_{shell,s}$  is always negative, while velocity in region (II)  $v_{shock}$  is negative prior to stagnation. In the strong-shock approximation, these relations are reduced to the expressions shown in Eq. (B9).

The shock pressure  $p_{shock}$  increases during the deceleration because of an increase in  $\rho_{shell}$  (due to the shell convergence) and the deceleration of the shocked shell (which leads to a reduction in  $|v_{shock}|$ ). The rate of increase in  $p_{shock}$  is reduced, on the other hand, by the deceleration of the unshocked shell and, consequently, a reduction in  $|v_{shell,s}|$ . These effects are discussed in details next.

The density increase in region (I) caused by convergence of the unshocked shell is described by the mass-conservation Eq. (B13), which leads to

$$\rho(m, t) \simeq \rho_0(m) \left[ \frac{r_0(m)}{r(m, t)} \right]^2 \Sigma^{-1}, \quad (51)$$

where

$$\Sigma = 1 + 4\pi\rho_0(m)r_0(m)^2 \int^t \frac{\partial v}{\partial m} dt, \quad (52)$$

$\rho_0(m)$  and  $r_0(m)$  are the shell density and position as functions of mass coordinate at the beginning of shell deceleration. For a flat velocity profile  $v$  in region (I),  $\partial v/\partial m \simeq 0$ ,

leading to a  $\rho \sim 1/r^2$  shell density increase with convergence. The actual velocity gradient is positive [the outer part of the shell in region (I) decelerates after Eqs. (42) and (43) are satisfied], reducing the rate of the density increase of the incoming shell. As shown in Appendix B [see Eq. (B12)], the velocity gradient at the time when the ablation front stops accelerating is proportional to the shell sound speed. The velocity gradient increases farther, while the peak shell pressure moves inside the shell due to convergence effects. Neglecting the latter effect and substituting Eq. (B12) into Eq. (52) yield

$$\Sigma \simeq 1 + 4\pi C_d \frac{c_{s0}}{M} (t - t_d) \rho_0(m) r_0(m)^2,$$

where the numerical coefficient  $C_d = \sqrt{2(2 - 3\beta/5)/(5 - \beta)}$  ranges from 0.8 to 0.9 for the values of  $\beta$  relevant to direct-drive implosions [see the discussion after Eq. (A4)],  $c_{s0}$  is the shell sound speed at the beginning of deceleration, and  $t_d$  is the starting time of the shell deceleration.

The reduction in the shocked shell velocity  $|v_{\text{shock}}|$  is calculated by relating it to the convergence rate of the hot spot (see Sec. V of Appendix B),

$$v_{\text{shock}} = \dot{R}_{\text{hs}} \left( 1 + \frac{M_s}{3\rho_{\text{shock}0} V_{\text{hs}0}} \right), \quad (53)$$

where  $R_{\text{hs}}$  is obtained by solving Eq. (47).

The velocity slowdown in the unshocked region (region I in Fig. 22) is calculated using the momentum conservation equation  $dv_{\text{shell}}/dt \sim -S_{\text{shock}} \partial p / \partial m$ , where the pressure is obtained by substituting Eq. (51) into  $p \sim \rho^{5/3}$ . The resulting pressure gradient takes the form

$$\frac{\partial p}{\partial m} \simeq \left( \frac{r_0}{r} \right)^{10/3} \Sigma^{-8/3} \left[ \frac{\partial p_0}{\partial m} + \frac{5p_0}{6\pi\rho_0 r_0^3} \right] - \left( \frac{r_0}{r} \right)^{13/3} \Sigma^{-2/3} \frac{5p_0}{6\pi\rho_0 r_0^3}. \quad (54)$$

The second term in Eq. (54) grows faster with convergence than the first term, leading to a negative pressure gradient and deceleration of the unshocked shell. This shows that the convergence effects decelerate the incoming shell in region (I) even before its interaction with the return shock. If not accurately modeled, such a deceleration can further reduce the stagnation pressure by decreasing  $v_{\text{imp}}$  in Eq. (24).

The set of Eqs. (47)–(53), together with the dependence of the hot-spot pressure on shell convergence [see Eq. (25)], defines the deceleration model. It can be used to study the effects of different implosion parameters on the peak hot-spot pressure. Next, using the deceleration model, simplified scaling laws for the hot-spot pressure and shocked mass are derived in Sec. IV C to guide physical understanding of deceleration dynamics.

In summary, the maximum hot-spot pressure depends on the convergence ratio of the shocked shell, which, in turn, depends on the shell deceleration rate. The larger the pressure gradient inside the shocked shell (larger difference

between  $p_{\text{hs}}$  and  $p_{\text{shock}}$ ) and the smaller the rate of increase in the shocked mass ( $dM_s/dt$ ), the larger the shell deceleration rate and the smaller the final convergence ratio of the shell. The pressure gradient increases and the rate of increase in the shocked mass decreases if the density and velocity of the incoming shell are reduced (due to preheat or RT growth). The pressure gradient is also increased in implosions with larger vapor mass and pressure at the onset of shell deceleration.

### C. Implosion scaling laws

The models described in Subsection IV B suggest the following simplified description of shell deceleration and hot-spot formation: The hot-spot pressure keeps increasing until the shell material overtaken by the return shock (region II in Fig. 22) stagnates. If the duration of shell deceleration is  $\Delta t_{\text{dec}}$ , then Eq. (47) gives

$$\frac{v_{\text{imp}}}{\Delta t_{\text{dec}}} \sim S_{\text{hs}} (p_{\text{hs}} - p_{\text{shock}}) / M_s. \quad (55)$$

The shell mass overtaken by the shock (the shocked mass), according to Eq. (B9), is

$$\frac{M_s}{\Delta t_{\text{dec}}} \sim \frac{p_{\text{shock}}}{v_{\text{imp}}} S_{\text{shock}}. \quad (56)$$

Eliminating the mass  $M_s$  and the time  $\Delta t_{\text{dec}}$  from Eqs. (55) and (56) yields a relation between the hot-spot and shock pressures

$$p_{\text{hs}} \sim p_{\text{shock}} (1 + S_{\text{shock}} / S_{\text{hs}}). \quad (57)$$

Since  $S_{\text{shock}} \geq S_{\text{hs}}$ , the hot-spot pressure is more than twice larger than the pressure at the shock front,

$$p_{\text{hs}} \gtrsim 2p_{\text{shock}} \sim \rho_{\text{shell}} v_{\text{imp}}^2. \quad (58)$$

Neglecting the velocity gradient inside the unshocked shell, the density increase caused by the shell convergence becomes [see Eq. (51)]

$$\rho_{\text{shell}} \sim \rho_{\text{shell}0} \left( \frac{R_{\text{hs}0}}{R_{\text{hs}}} \right)^2, \quad (59)$$

and the hot-spot pressure scales with the convergence ratio as [see Eq. (26)]

$$p_{\text{hs}} = p_{\text{hs}0} \left( \frac{R_{\text{hs}0}}{R_{\text{hs}}} \right)^5. \quad (60)$$

Eliminating  $p_{\text{hs}}$  from Eqs. (58) and (60) gives the hot-spot convergence ratio during deceleration,

$$\frac{R_{\text{hs}0}}{R_{\text{hs}}} \sim \left( \frac{\rho_{\text{shell}0} v_{\text{imp}}^2}{p_{\text{hs}0}} \right)^{1/3}. \quad (61)$$

Equation (61) shows that having a larger vapor pressure (because of a larger initial vapor mass, higher shell adiabat,

or ablator-to-vapor mix) at the beginning of the shell deceleration leads to a lower hot-spot convergence ratio.

Combining Eq. (61) with Eq. (26) gives a scaling for the hot-spot pressure

$$p_{\text{hs}} \sim p_{\text{hs0}} \left( \frac{\rho_{\text{shell0}} v_{\text{imp}}^2}{p_{\text{hs0}}} \right)^{5/3} = (\rho_{\text{shell0}} v_{\text{imp}}^2)^{5/3} p_{\text{hs0}}^{-2/3}. \quad (62)$$

Similar to Eq. (61), Eq. (62) also demonstrates the benefit of reducing the vapor pressure  $p_{\text{hs0}}$  at the start of the shell deceleration. Since the vapor pressure at that time equals the shell pressure (which scales as the ablation pressure  $p_a$ ),  $p_{\text{hs0}} = p_{\text{shell0}} \sim p_a$  and  $p_{\text{shell0}} \sim \alpha_{\text{shell}} \rho_{\text{shell0}}^{5/3}$ , Eq. (62) reduces to

$$p_{\text{hs}} \sim \frac{p_a^{1/3} v_{\text{imp}}^{10/3}}{\alpha_{\text{shell}}}. \quad (63)$$

Using Eq. (63) in Eq. (2) leads to a scaling for the minimum shell kinetic energy required for ignition,

$$E_{\text{k,min}} \sim v_{\text{imp}}^{-20/3} p_a^{-2/3} \alpha_{\text{shell}}^2. \quad (64)$$

This scaling is similar to that obtained using simulation results.<sup>47</sup>

Because of its limited region of validity, the scaling law given in Eq. (63) should be used mainly as a guiding tool in understanding the effects of different implosion parameters on the shell properties at peak compression. The limitations in applicability of Eq. (63) include the following: First, according to Eq. (51), the dependence of the shell density on the convergence ratio is somewhat weaker than that shown in Eq. (59). This leads to a smaller power index in the velocity dependence than shown in Eq. (63).

Second, the scaling law shown in Eq. (63) assumes unlimited mass in the unshocked shell (region I in Fig. 22). As the implosion velocity increases or the shell adiabat decreases, the shocked mass predicted by Eq. (56) increases, and Eq. (63) becomes invalid when  $M_s$  exceeds the total shell mass  $M$ . To show this, the shocked mass is estimated by using the energy-conservation equation. The kinetic energy of the shocked shell,  $M_s v_{\text{imp}}^2/2$ , is converted at stagnation into the internal energy of the hot spot,  $3/2 p_{\text{hs}} V_{\text{hs}}$ , and the shocked shell energy,  $E_{\text{shell}} = 3/2 \int p dV$ . The latter is estimated by using the expression for the pressure profile shown in Eq. (B1)

$$E_{\text{shell}} = 3/2 M \int_0^{M_s/M} \frac{p(m')}{\rho(m')} dm', \quad (65)$$

where  $m' = m/M$  is the normalized mass coordinate,  $\rho = (p/\mu \alpha_{\text{shock}})^{3/5}$ , and  $\alpha_{\text{shock}}$  is the adiabat of the shocked shell. It can be shown that the integral in Eq. (65) scales as  $E_{\text{shell}} \sim M_s v_{\text{imp}}^2$ . As a result, energy conservation leads to

$$M_s v_{\text{imp}}^2 \sim p_{\text{hs}} V_{\text{hs}}, \quad (66)$$

which, in combination with Eq. (58), gives

$$M_s \sim \rho_{\text{shell}} V_{\text{hs}}. \quad (67)$$

Substituting the scalings for the shell density and the hot-spot volume from Eqs. (59) and (61) gives

$$M_s \sim \frac{p_a^{11/15} R_{\text{hs0}}^3}{\alpha^{2/5} v_{\text{imp}}^{2/3}}. \quad (68)$$

The scaling for the shocked mass must be compared with the scaling for the total shell mass. The latter is derived by combining the relations between the initial shell radius  $R_0$  and the implosion velocity,  $R_0 \sim v_{\text{imp}} t_{\text{imp}}$ , and the shell mass and the ablation pressure (Newton's law),  $M v_{\text{imp}}/t_{\text{imp}} \sim R_0^2 p_a$ . The implosion time can be written as the ratio of the laser energy and laser power,  $t_{\text{imp}} \sim E_{\text{laser}}/R_0^2 I$ , where  $I$  is the incident laser intensity. This gives

$$M \sim \frac{p_a E_{\text{laser}}}{v_{\text{imp}} I}, \quad R_0 \sim \left( \frac{E_{\text{laser}} v_{\text{imp}}}{I} \right)^{1/3}. \quad (69)$$

Substituting Eq. (69) into Eq. (68) and assuming that the scalings of  $R_{\text{hs0}}$  and  $R_0$  are the same yield

$$\frac{M_s}{M} \sim \frac{v_{\text{imp}}^{4/3}}{\alpha^{2/5} p_a^{4/15}}, \quad M_s \sim \frac{p_a^{11/15} v_{\text{imp}}^{1/3} E_{\text{laser}}}{\alpha^{2/5} I}. \quad (70)$$

To increase  $v_{\text{imp}}$  for a given laser energy and intensity, the shell mass, according to Eq. (69), must be reduced. The shocked mass, however, increases with  $v_{\text{imp}}$  [see Eq. (70)]. Consequently, as  $M$  reduces and  $v_{\text{imp}}$  increases, Eq. (70) becomes invalid at some point when  $M_s$  exceeds  $M$ . This defines the validity region for the scaling laws shown in Eqs. (63) and (70).

In summary, the adiabatic condition of the hot-spot pressure evolution,  $p_{\text{hs}} \sim R^{-5}$ , leads to a strong dependence of the stagnation pressure in the implosion velocity and inflight adiabat,  $p_{\text{hs}} \sim v_{\text{imp}}^{10/3} / \alpha_{\text{shell}}$ .

## V. RELATING TARGET PERFORMANCE TO THE UNSHOCKED MASS

In optimizing the target design, there is a trade-off between maximizing 1-D performance and controlling hydrodynamic instabilities. The 1-D target performance improves if a larger fraction of the shell is overtaken by the return shock at the hot-spot stagnation. This leads to a larger shocked mass and larger fraction of the shell kinetic energy being converted into the hot-spot internal energy. Equation (70) shows that increasing the implosion velocity and reducing the shell adiabat result in a larger shocked mass and, according to Eq. (63), a higher hot-spot pressure.

The benefits of reducing the shell adiabat in raising the shell density and shocked mass are limited, however, by the RT growth at the ablation front during the acceleration. The lower-adiabat shells are more susceptible to the perturbation growth because of reduced ablative stabilization.<sup>6</sup> The larger instability growth leads to a larger region of relaxed density at the outer part of the shell (see Fig. 23). As the outgoing shock travels through such a lower-density mix region during shell deceleration, the shock pressure,  $p_{\text{shock}} \sim \rho_{\text{shell}} v_{\text{imp}}^2$ , is

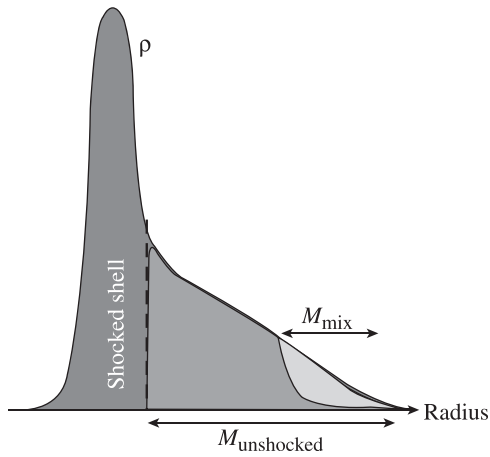


FIG. 23. A sketch of the shell density at peak compression. The region marked with “ $M_{\text{mix}}$ ” indicates the outer part of the shell with the relaxed density due to hydrodynamic instability growth.

reduced, and the shell deceleration rate increases [see Eq. (55)]. The stronger deceleration force stops the shell while the hot spot is at a larger radius, leading to a reduction in the shocked mass and hot-spot pressure. This also follows from Eq. (62), which shows that  $p_{\text{hs}} \sim \rho_{\text{shell}}^{5/3}$ .

The target performance degradation depends on the mass (or size) of the mix region that contributes to the shocked mass at stagnation. If the hot spot stagnates before the return shock reaches the mix zone, as illustrated in Fig. 23, the effect of the RT growth is small. And, vice versa, if the shocked mass at stagnation includes a significant fraction of the mixed mass, the hot-spot convergence and peak pressure are reduced. This is illustrated in Fig. 24, which plots the results of a series of *LILAC* simulations of cryogenic implosions where the shell density was artificially relaxed (without changing the shell velocity or mass) at the beginning of shell deceleration. A reduction in the hot-spot pressure in these simulations depends on the fraction of relaxed material in the shocked mass at stagnation. When the return shock at peak compression has not reached yet the outer part of the shell where the material is mixed due to hydrodynamic instability growth (and the mass density, therefore, is relaxed), the ratio  $(M_{\text{mix}} - M_{\text{unshocked}})/M_{\text{shocked}}$  is negative and the effect of the mix on the target performance is negligible. On the other hand, when the mix region extends to

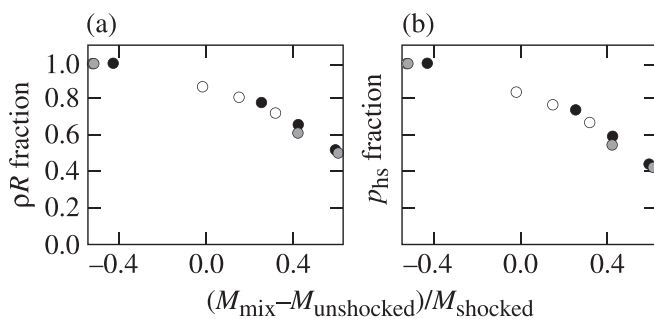


FIG. 24. *LILAC* predictions of (a) the areal density and (b) the peak hot-spot pressure fractions as functions of the relaxed (mixed) shell fraction in the shocked mass at peak compression. Different symbols indicate different target designs.

include 60% of the shocked mass (as calculated in the no-mix run), the peak areal density is reduced by 50% and the peak pressure by 60% compared with the results of the no-mix simulation.

To quantify the effects of hydrodynamic instability growth on the observed target performance, contours of the measured areal densities normalized to 1-D predictions are shown (see Fig. 25) in the adiabat/unshocked mass parameter space. Since the areal density in an experiment is inferred using nuclear reaction products, the unshocked mass is calculated at the bang time. A stability boundary can be identified (shown with a thick solid line) that separates the region where more than 85% of the predicted areal density is measured and the region where the effect of instability growth is significant enough to reduce the observed areal densities.

According to Fig. 25, the measured areal-density fraction, for a given adiabat, increases with the unshocked mass. The 1-D-predicted values are achieved only if  $\alpha > 2.3$ . For these implosions, a vertical line representing designs with a fixed adiabat always intersects with the stability boundary. An  $\alpha = 3$  line, for example, intersects the stability boundary at  $M_{\text{mix}}(3) \simeq 7.5 \mu\text{g}$ , indicating that the shell compression is not degraded if the unshocked mass is larger than  $M_{\text{mix}}$ . Then, according to Fig. 24,  $M_{\text{mix}}$  is equal to the mass of relaxed density at the ablation front (mix mass). Consequently, the stability boundary represents the points where the unshocked mass equals the mix mass. To highlight the dependence of the mix mass on shell adiabat (obtained as

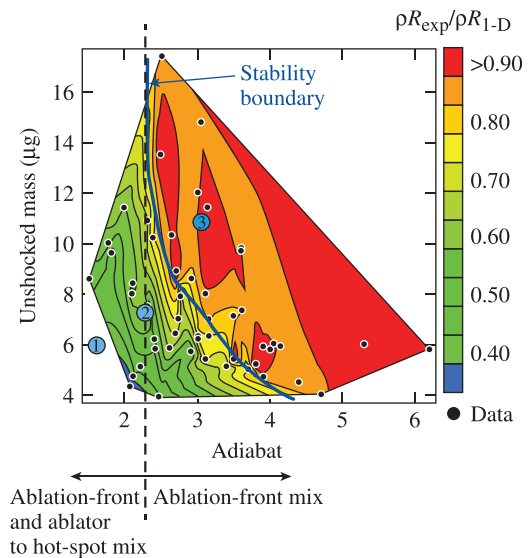


FIG. 25. Contour map of the measured areal-density reduction relative to 1-D predictions. The unshocked mass (see Fig. 23) is calculated at bang time using *LILAC*. The stability boundary (see also caption to Fig. 14) is shown with the thick solid line. The dashed line separates the parameter space into a region ( $\alpha > 2.3$ ) where a vertical line representing implosions with a fixed adiabat intersects with the stability boundary at  $M_{\text{unshocked}} = M_{\text{mix}}$  and a region ( $\alpha < 2.3$ ) where the mix extends over the whole shell and measured areal densities are below 70% of 1-D predictions for any values of the unshocked mass. The excessive bubble growth caused by hydrodynamic instabilities breaks up the shells with  $\alpha < 2.3$  early during acceleration, causing the ablator mixing into the hot spot. The blue numbered circles correspond to (1) nominal CBET, (2) 1/2 CBET, and (3) no CBET designs shown in Fig. 27 and Table III.



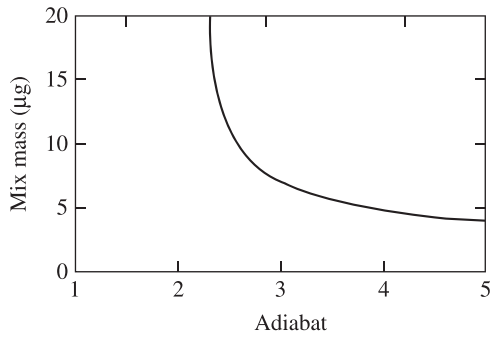


FIG. 26. Mix mass  $M_{\text{mix}}$  as function of shell adiabat. The mix mass equals to the total shell mass for  $\alpha < 2.3$  since these shells are broken during the acceleration.

a fit to the experimental data presented in Fig. 25), the stability boundary is shown again in Fig. 26.

For implosions with  $\alpha < 2.3$  (to the left of the dashed vertical line in Fig. 25), a line of constant adiabat never intersects the stability boundary. This indicates that, in addition to the density relaxation at the ablation front, a different performance-degradation mechanism limits the target compression. A possible mechanism is suggested by the observed correlation between the measured x-ray emission from the target core and the shell adiabat. This is shown in Fig. 8 of Ref. 30, where the calculated and measured core emission in the sensitivity range of the gated x-ray imager<sup>37</sup> (4 to 7 keV) are plotted for different values of the shell adiabat. Enhanced emission is observed in the implosions with  $\alpha < 2.3$  and can be explained by the presence of carbon in the hot spot at the peak of x-ray production. This is due to shell breakup and the CD ablator penetrating into the vapor region during shell acceleration. The shell breakup increases the vapor mass and reduces the shell density. Both effects, as discussed in Sec. IV B, lead to an early shell deceleration and a significant reduction in the peak areal densities and hot-spot pressures.

Because the CD layer in direct-drive cryogenic implosions on OMEGA is totally ablated by the end of the drive pulse, the only mechanism capable of mixing the CD ablator into the vapor region is the nonlinear evolution of localized surface defects (or ice features) at the early stages of the implosion.<sup>43</sup> Bubbles of the lower-density material break shell integrity at the beginning of the shell acceleration, bringing the cold fuel, ablator material, and ablated plasma into the vapor region and compromising target performance. This result suggests that the bubble velocity  $v_{\text{bubble}} \sim \sqrt{d_{\text{bubble}}g}$  (where  $g$  is the shell acceleration and  $d_{\text{bubble}}$  is the bubble diameter) in the implosions with  $\alpha < 2.3$  exceeds the rate of increase in the in-flight shell thickness.

## VI. TOWARD DEMONSTRATION OF IGNITION HYDRODYNAMIC EQUIVALENCE IN CRYOGENIC IMPLOSIONS ON OMEGA

### A. The hot-spot pressure requirement for an igniting target

As shown in Sec. III, cryogenic implosions on OMEGA have reached maximum and neutron-averaged hot-spot pressures of up to  $\sim 40$  Gbar and  $\sim 30$  Gbar, respectively. The

pressure requirement for an ignition demonstration on the NIF can be derived using Eq. (3), which, with the help of Eq. (25), reduces to

$$\left(\frac{p_{\text{hs}}}{100 \text{ Gbar}}\right)^{4/5} \left(\frac{p_{\text{hs}0}}{100 \text{ Gbar}}\right)^{1/5} > \frac{100 \mu\text{m}}{R_{\text{hs}0}}. \quad (71)$$

Assuming that the convergence of the original vapor mass contributes the most to the vapor pressure at the beginning of deceleration,  $p_{\text{hs}0}$  (see Sec. IV B 1), Eq. (32) is used to obtain

$$p_{\text{hs}0} = p_{\text{a}0} F \left( \frac{\rho_{\text{v}0}}{\rho_{\text{ice}0}} \right) \left( \frac{R_{\text{v}0}}{R_{\text{hs}0}} \right)^5, \quad (72)$$

where  $R_{\text{v}0}$  is the initial (undriven) size of the vapor region,  $\rho_{\text{v}0}$  and  $\rho_{\text{ice}0}$  are the initial densities of the vapor and the main fuel, respectively,  $p_{\text{a}0}$  is the ablation pressure at the beginning of acceleration, and the function  $F(x)$  is defined as

$$F(x) = \frac{x}{4^{5/3}} [1 + 2\sqrt{5}(1 - x^{1/5})]. \quad (73)$$

At the DT triple-point,  $\rho_{\text{v}0} \simeq 0.6 \text{ mg/cm}^3$  and  $\rho_{\text{ice}0} \simeq 0.25 \text{ g/cm}^3$ , so  $F(2.4 \times 10^{-3}) \simeq 10^{-3}$ . Using Eq. (68) to calculate the initial vapor radius gives

$$R_{\text{v}0} \simeq 0.85 \left( \frac{E_{\text{laser}} v_{\text{imp}}}{4\pi I} \right)^{1/3}. \quad (74)$$

The numerical factor in Eq. (74) is obtained by fitting Eq. (68) to the results of *LILAC* simulations. Combining Eqs. (71)–(74) leads to the following requirement for the minimum hot-spot pressure in an igniting target

$$p_{\text{hs}} \geq 120 \text{ Gbar} \left( \frac{100 \text{ Mbar}}{p_{\text{a}0}} \right)^{1/4} \times \left( \frac{E_{\text{laser}}}{1.5 \text{ MJ}} \frac{v_{\text{imp}}}{3.7 \times 10^7 \text{ cm/s}} I_{15}^{-1} \right)^{-5/12}, \quad (75)$$

where  $I_{15}$  is the incident laser intensity in  $10^{15} \text{ W/cm}^2$ . Equation (75) shows that the cryogenic implosions, hydrodynamically equivalent to an igniting target on the NIF, need to achieve central pressures in excess of  $\sim 100$  Gbar. So, the maximum hot-spot pressures inferred in cryogenic implosions on OMEGA are lower by a factor of 2 to 3 than what is required for the ignition demonstration on the NIF.

According to Figs. 14 and 18, the reduction in the central pressure is larger than the reduction in areal density. More than 85% of the 1-D-predicted  $\rho R$  values are observed in the implosions without significant ablator mixing into the vapor region or density relaxation at the ablation front. In contrast, the inferred central pressures in such implosions are reduced by more than 60%. This is a result of the hot-spot distortion growth during the shell deceleration. When integrity of the in-flight shell is not compromised by the RT growth, a large fraction of predicted areal density is observed if the mix mass at the ablation front does not exceed the unshocked mass at bang time (see Fig. 25). Perturbations at the inner edge of the shell (caused by feedthrough from the

ablation front) grow during the deceleration due to the RT instability, as the pressure and density gradients have the opposite signs at the inner surface of the shell. This growth leads to an increase in the hot-spot volume and the surface area. The larger surface area of the colder shell leads to enhanced thermal conduction losses from the hotter central region and a larger mass ablation from the shell into the hot spot. This reduces the hot-spot temperature and truncates the neutron production before the hot spot reaches its minimum volume. Since the hot-spot pressure is inferred using the nuclear diagnostics, the early burn truncation prevents sampling the pressures at higher hot-spot convergence ratios, reducing the inferred pressure values.

The other multidimensional effect that leads to a reduction in the hot-spot pressure is the growth of the nonradial component of the flow resulted from shell's distortion growth. Such nonradial flow reduces the fraction of the shell kinetic energy that is converted into hot-spot internal energy.<sup>48</sup> In a spherically symmetric implosion, the full kinetic energy of the shocked shell,  $M_s v_{\text{shell}}^2/2$ , is converted into the internal energy of the hot spot and shocked shell,

$$\frac{1}{2} M_s v_{\text{shell}}^2 \rightarrow \frac{3}{2} p_{\text{hs}} V_{\text{hs}} \text{ (spherically symmetric implosion).}$$

In the presence of asymmetries, there is a residual fluid motion in the shocked region because of the RT growth. If  $M_s v_{\text{RT}}^2/2$  is the shell kinetic energy associated with such motion, the energy balance gives

$$\frac{1}{2} M_s v_{\text{shell}}^2 \rightarrow \frac{3}{2} p_{\text{hs}} V_{\text{hs}} + \frac{1}{2} M_s v_{\text{RT}}^2 \text{ (asymmetric implosion),}$$

leading to a reduction in  $p_{\text{hs}} V_{\text{hs}}$  compared to a symmetric implosion. In addition, only the velocity component normal to the shock front,  $v_{\text{shell}\perp}$ , contributes to the shock pressure shown in Eqs. (B7) and (B58), so only a fraction of the incoming shell dynamic pressure is converted into shock pressure  $p_{\text{shock}}$

$$\frac{4}{3} \rho_{\text{shell}} v_{\text{shell}\perp}^2 \rightarrow p_{\text{shock}} \text{ (asymmetric implosion).}$$

This reduces the shock pressure and increases the pressure gradient inside the shocked shell, leading to a larger deceleration force, a larger hot-spot volume, and a smaller hot-spot pressure at peak compression.

## B. Direct-drive target designs with improved shell stability

Since the numerical simulations and the experimental data suggest that only  $\sim 40\%$  of the 1-D-predicted peak pressures are observed in the presence of perturbation growth, demonstrating ignition hydrodynamic scaling on OMEGA with peak pressures of  $\sim 100$  Gbar requires 1-D designs reaching  $p_{\text{hs}} \sim 200$  Gbar at stagnation. Such a design is shown in Fig. 27. The pulse shape is shown with the solid lines and the target is labeled “nominal CBET.” Driven at a peak laser intensity of  $9.5 \times 10^{14} \text{ W/cm}^2$ , it reaches an implosion velocity of  $3.7 \times 10^7 \text{ cm/s}$ . The calculated unshocked mass, fuel adiabat, and in-flight aspect ratio are  $m_{\text{unshocked}} = 6 \mu\text{g}$ ,  $\alpha = 1.65$ ,

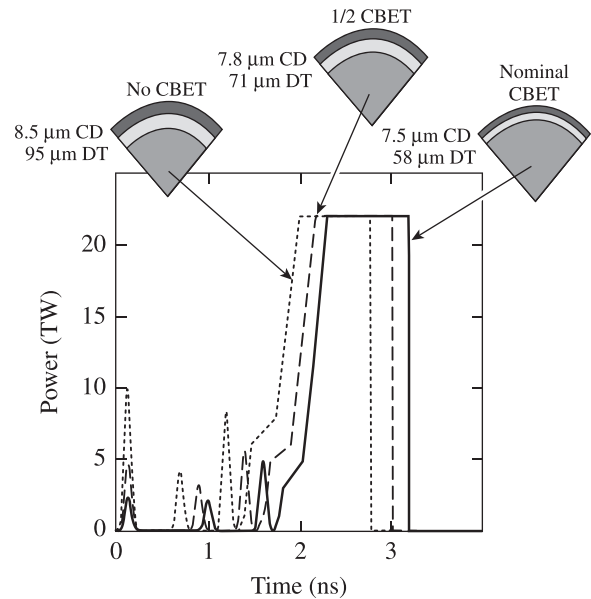


FIG. 27. OMEGA cryogenic target designs with 1-D central pressures of 180 Gbar at stagnation, an implosion velocity of  $3.7 \times 10^7 \text{ cm/s}$ , and neutron-averaged areal density of  $\sim 300 \text{ mg/cm}^2$ .

and IFAR = 30, respectively. Such a design, according to Figs. 14(b) and 25 (see the blue circle labeled “1”), is unstable, however, assuming the nonuniformity seeds currently present in OMEGA cryogenic implosions. The shell stability must, therefore, be improved to demonstrate hydrodynamic equivalence. This can be achieved by reducing the level of the nonuniformity seeds [which will move the stability boundary shown in Figs. 14(b) and 25 to a region with lower adiabat values and unshocked shell masses and higher IFARs] and by increasing the hydrodynamic efficiency (the ratio of shell kinetic energy to the incident laser energy) of the imploding target. At higher hydrodynamic efficiency of the laser drive, the required peak in the hot-spot pressure can be reached in implosions with higher adiabat values and unshocked masses and lower IFARs, moving the hydroequivalent design into the stable region in the adiabat/IFAR and adiabat/unshocked mass parameter spaces.

Identifying the dominant nonuniformity seed is currently underway at LLE. Possible sources include target defects introduced during the fill, cooling, and cryogenic fuel layer formation, as well as early laser shinethrough and interaction of the first shock with modulations in the solid-state properties of the ablator.

Improving the shell's stability by raising the adiabat and lowering IFAR (keeping the hot-spot pressure fixed) can be achieved [according to the scaling shown in Eq. (63)] by increasing the ablation pressure  $p_a$ . An important factor limiting the laser absorption and ablation pressure in direct-drive implosions is CBET.<sup>12</sup> Thus, the most efficient way to raise  $p_a$  is to mitigate the CBET. LLE is currently pursuing several mitigation approaches,<sup>12,49</sup> including reducing the laser-beam size relative to the target size, increasing the laser bandwidth, and introducing layers of mid-Z materials (Si, for example) inside the ablator. The benefit of CBET mitigation on implosion characteristics is illustrated by a comparison of the

TABLE III. Summary of the shell parameters for the designs shown in Fig. 27. All designs have peak hot-spot pressure of 180 Gbar, the neutron-averaged areal density of 300 mg/cm<sup>2</sup>, and the implosion velocity of  $3.7 \times 10^7$  cm/s.

Parameters	Nominal CBET	1/2 CBET	No CBET
Ablation pressure (Mbar)	138	162	213
IFAR	30	23	17
Adiabat	1.6	2.2	3.2
Unshocked mass ( $\mu\text{g}$ )	6	7.5	11.3
Total unablated shell mass ( $\mu\text{g}$ )	17.4	19.4	23.7
Initial shell mass (ablator and DT) ( $\mu\text{g}$ )	47.1	53.1	63.4

designs with various fractions of the laser-deposition reduction caused by CBET (shown in Fig. 27). The maximum hot-spot pressure, shell velocity, and peak areal density in these designs are kept fixed. The effect of CBET is varied in simulations by introducing a multiplicative factor in front of the growth rate for the stimulated Brillouin scattering (SBS)<sup>14</sup> that governs the CBET (the design labeled “1/2 CBET” is simulated using a factor of 1/2 in front of the SBS growth rate, and the simulation of the “no CBET” design has no effect of the CBET). Reducing CBET increases the ablation pressure, leading to a hydroequivalent design with an increased fuel mass and adiabat and reduced IFAR. The shell parameters for these designs are summarized in Table III.

The shell IFAR, fuel adiabat, and unshocked mass for the three designs are indicated in Fig. 28 by the solid circles. Also shown are best fits to the simulation data. The IFAR scales with the ablation pressure as  $\text{IFAR} \sim p_a^{-1.36}$ , while the fuel adiabat and the unshocked mass scale as  $p_a^{1.5}$ .

The improvement in shell stability by reducing CBET is also demonstrated in Fig. 25 where positions of Nominal CBET (blue circle labeled “1”), 1/2 CBET (blue circle “2”),

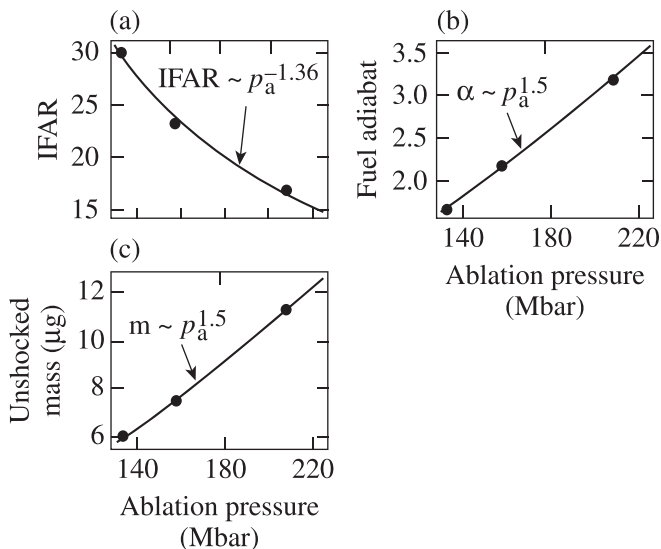


FIG. 28. (a) Inflight shell IFAR<sub>2/3</sub>, (b) inflight fuel adiabat, and (c) the unshocked mass at the time of peak neutron production as functions of ablation pressure for the designs shown in Fig. 27. The symbols show the simulation results, and the solid lines represent best fits to the simulations.

and No CBET (blue circle “3”) designs are shown in the unablated mass/adiabat parameter space.

### C. CBET mitigation strategies

Different CBET mitigation strategies are compared by calculating the ablation pressure using the CBET model implemented in *LILAC*.<sup>12</sup>

#### 1. Reduced laser beam size and increased laser wavelength separation

As discussed in Refs. 12 and 49, reducing the laser beam size relative to the target size mitigates the effect of CBET. Figure 29 shows the predicted ablation pressure in OMEGA cryogenic implosions as a function of the ratio of the beam radius (defined as the radius of a region with 95% of beam energy),  $R_{\text{beam}}$ , to the initial target radius,  $R_{\text{target}}$ .  $R_{\text{beam}}/R_{\text{target}} \sim 0.8$  is equivalent to the “1/2 CBET” design, and reducing the beam radius to  $R_{\text{beam}} \sim 0.6R_{\text{target}}$  leads to the ablation pressure similar to that of the “no CBET” design shown in Fig. 27. This does not mean, however, that CBET is completely suppressed at such a beam radius. There are two effects that increase the ablation pressure when the beam size is reduced.<sup>12</sup> The first is a reduction in CBET, and the second is a decrease in the average angle of incidence in the laser illumination (as discussed in the context of the original zooming designs in Ref. 50). The beam rays, which have smaller incidence angles to the target-surface normal, propagate farther toward the higher electron densities,<sup>14</sup> depositing their energy more efficiently. Consequently, a combination of the CBET reduction and a decrease in the incidence angles leads to matching the ablation pressure in the  $R_{\text{beam}}/R_{\text{target}} \simeq 0.6$  design with the pressure when the CBET is fully mitigated at  $R_{\text{beam}}/R_{\text{target}} \simeq 1$ .

The smaller beams, however, enhance illumination non-uniformity because of the reduced beam overlap. This also increases the sensitivity of the target design to power imbalance and beam mistiming. To mitigate this problem, a two-stage zooming scheme has been proposed,<sup>49</sup> wherein  $R_{\text{beam}}/R_{\text{target}} \simeq 1$  is used until the onset of the main drive, and  $R_{\text{beam}}/R_{\text{target}} < 0.7$  is used thereafter. Controlling the

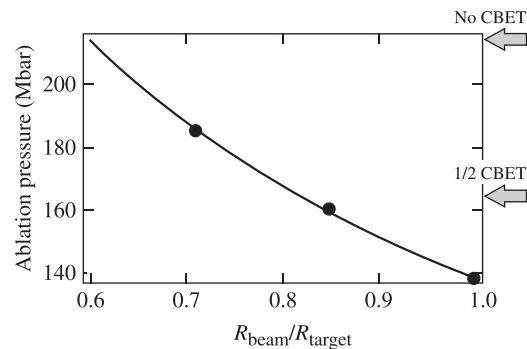


FIG. 29. The ablation pressure (calculated after the ablation front has converged by factor 2.5) as predicted by *LILAC* (including the CBET effect) versus the ratio of the beam radius to the target radius. Points show simulation results and the solid line is the best fit to the simulations. The arrows indicate the ablation pressure with 1/2 CBET and without CBET for  $R_{\text{beam}} = R_{\text{target}}$ .

single-beam uniformity for modes  $20 < l < 100$  is the main challenge for this mitigation scheme. The target design optimization involves finding a compromise between improving the target stability properties (by reducing the IFAR and increasing the adiabat and unshocked mass) and increasing illumination nonuniformity seeds. Several zooming implementation options are currently being pursued on OMEGA.

Mitigating CBET by increasing the **laser wavelength separation**<sup>12</sup> requires the separation in excess of  $5 \text{ \AA}$  at a laser wavelength of  $\lambda = 351 \text{ nm}$ . The CBET model implemented in *LILAC* suggests<sup>12</sup> that this gives an effective reduction in the SBS gain by a factor of 2, leading to the target design “1/2 CBET” shown in Fig. 27. Currently, this is considered to be the best option in mitigating CBET in the polar-drive implosions on the NIF.

## 2. Multilayer ablators

Introducing a mid-Z layer (such as Si) inside the ablator leads to several beneficial effects. First, having a higher-Z material inside the laser-absorption region increases inverse bremsstrahlung absorption, as discussed in Sec. II. Consequently, even if the laser-deposition reduction caused by CBET is held constant, higher-Z ablators lead to higher absorption. This also increases the coronal temperature, which, in turn, reduces the SBS gain that governs the CBET.

An additional benefit in using a mid-Z layer is mitigation of the TPD instability. As mentioned in Sec. II and discussed in detail in Ref. 17, the higher-Z plasma at quarter-critical electron density reduces the ion-wave damping rate, leading to a reduction in TPD growth. An increase in the coronal temperature caused by the higher laser absorption also mitigates TPD instability.

Higher-Z materials have several disadvantages, such as low hydrodynamic efficiency, radiation losses, and radiation preheat (see discussion in Sec. II), which diminish the benefits of the CBET reduction. For these reasons, the mid-Z layer (such as Si) is chosen to be thin. It is placed inside the lower-Z material to combine the higher laser absorption with the larger ablation efficiency of the innermost layer in the ablator. DT has the highest ablation efficiency (because of the large ratio of atomic mass to the ion charge), but the lowest ion charge and, therefore, the smallest inverse bremsstrahlung absorption. Having the mid-Z layer extended all the way to the DT layer causes either significant radiation preheat of the main fuel due to radiation from the plasma corona (if the layer is thick) or a significant loss in the laser absorption by depositing laser energy in the DT during the main pulse (if the layer is thin). Both reduce the benefits of having a higher ion charge in the plasma corona.

The best design option is to introduce an intermediate layer between the mid-Z layer and the DT ice. The material in this layer must have high ablation efficiency, while the ion charge must be larger than 1 to avoid significant losses in laser absorption. From a target-manufacturing point of view, beryllium is the best choice for this purpose.<sup>23</sup> A hydroequivalent multilayer design for OMEGA and the corresponding ignition design for the NIF are shown in Fig. 30. The OMEGA design is predicted to absorb 60% of the incident

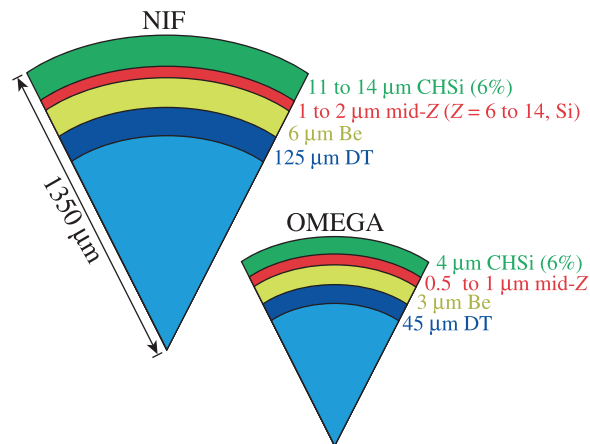


FIG. 30. Multilayer ignition design for the NIF (left) and hydroequivalent design for OMEGA (right). The outer plastic layer is doped with Si to reduce the laser imprint.<sup>51</sup>

laser energy. This compares with the 54% absorption achieved in the “nominal CNET” design of Sec. VI B. The higher absorption fraction results in an increase in the ablation pressure from 138 Mbar to 147 Mbar, fuel adiabat from  $\alpha \simeq 1.6$  to  $\alpha \simeq 2$ , and the unshocked mass from  $6 \mu\text{g}$  to  $7 \mu\text{g}$ . These values indicate a moderate improvement in stability properties compared with those in the “nominal CBET” design shown in Table III. The corresponding NIF multilayer design, shown in Fig. 30, is predicted to ignite in 1-D and produces a gain of 5 if no additional CBET mitigation strategies are used. Employing a laser wavelength separation of  $5 \text{ \AA}$  in the UV further reduces CBET and increases the gain to 20. Additional strategies that increase the shell convergence and target gain are currently being considered at LLE.

Although much more work is required to validate the predicted benefits and to access the stability properties of the multilayer design, the first experiments performed on OMEGA using multilayer warm targets (with the cryogenic layer replaced by an extra layer of Be) have confirmed an increased coronal temperature compared with that in pure plastic shells.<sup>52</sup> The observed generation of suprathermal electrons caused by the TPD instability was also reduced in implosions with the multilayer targets.

## VII. CONCLUSIONS

The target performance of cryogenic implosions on OMEGA has been discussed. The implosion velocity was varied from  $2.2$  to  $3.8 \times 10^7 \text{ cm/s}$  and the fuel adiabat from 1.5 to 5. Based on the results of these experiments, the stability boundaries in the IFAR/adiabat and unshocked mass/adiabat parameter spaces were identified. The target designs operating in the stable region achieve more than 85% of the 1-D-predicted areal densities. The hot-spot pressures and yields are up to 35% and 40% of the predictions, respectively. The target performance of the implosions in this stability regime is well understood using *DRACO* simulations.

A measure of the effect of the ablative RT growth on target performance is the fraction of the mix-region mass (in the proximity of the ablation front) in the mass that has been shocked by the outgoing shock during target deceleration. If



this shock has not reached the mixed region at peak neutron production (the mix mass is smaller than the unshocked mass), the effect of the ablative RT mix on the measured areal density is small. The target yields and peak pressures are reduced in such implosions to  $\sim 30\%$  to  $40\%$  of the 1-D predictions because of nonuniformity growth during the shell deceleration.

To demonstrate ignition hydrodynamic equivalence, OMEGA implosions must reach central pressures in excess of 100 Gbar. With the current limitations in the laser absorption caused by CBET, the fuel adiabat in the hydroequivalent designs must be at  $\alpha < 2$  and the shell IFAR must be  $\sim 30$ , which are outside of the current shell-stability region. The target performance of designs with these parameters is significantly degraded with respect to 1-D predictions. 2-D simulations using the known sources of target and illumination nonuniformities also fail to reproduce the experimental data. This limited ability of the hydrodynamic simulations to explain the observables in the low-adiabat implosions on OMEGA is common to that in indirect-drive cryogenic implosions on the NIF.

To understand the factors limiting the target performance, simplified models describing the implosion dynamics have been developed. These models reveal that the vapor pressure evolution during the shell acceleration and the shell density relaxation caused by hydrodynamic instability growth, preheat, and material release from the inner surface of the shell are the main factors controlling the target performance. It was shown that 2-D *DRACO* simulations, which use the localized features on the target surface as the nonuniformity seed reproduce the observables for  $\alpha \simeq 2$  implosions. The shells in these simulations are totally broken and colder fuel from the shell, ablator material, and some of the hotter blow-off plasma are injected into the target center, significantly reducing the final shell convergence and hot-spot pressure.

Based on the analysis using the simplified models and the simulations including the localized defects, it has been concluded that ignition hydrodynamic equivalence can be achieved on OMEGA by making the cryogenic designs more robust against hydrodynamic instabilities. This requires a reduction in the nonuniformity sources and an increase in hydrodynamic efficiency by mitigating CBET. LLE is currently pursuing several CBET-mitigation strategies, including a reduced laser beam size relative to the target size, laser wavelength separation, and multilayer ablators.

## ACKNOWLEDGMENTS

This material is based upon work supported by the Department of Energy National Nuclear Security Administration under Award No. DE-NA0001944, the University of Rochester, and the New York State Energy Research and Development Authority. The support of DOE does not constitute an endorsement by DOE of the views expressed in this article.

## APPENDIX A: SHELL ACCELERATION MODEL

The momentum-conservation equation in the mass–time coordinate system has the form

$$\frac{\partial^2 r(m, t)}{\partial t^2} = -4\pi r(m, t)^2 \frac{\partial p(m, t)}{\partial m}, \quad (\text{A1})$$

where  $p$  is shell pressure,  $r$  is position,  $m$  is the mass coordinate defined as  $dm = 4\pi\rho r^2 dr$ , and  $\rho$  is mass density. A rigorous approach for finding  $r(m, t)$  requires solving a nonlinear partial differential equation by substituting  $p(m, t) = \mu\alpha(m, t)/[4\pi r^2(\partial r/\partial m)]^{5/3}$  into Eq. (A1). Here, the shell adiabat  $\alpha(m, t)$  varies with time during the shell acceleration because of secondary shocks, radiation, or suprathermal electron preheat, and  $\mu$  is defined in Eq. (19). Instead, an approximate solution of Eq. (A1) is obtained by using the following simplifications: First, the pressure profile inside the shell is written as a second-order polynomial in the mass coordinate,

$$p(m, t) \simeq p_a(t)[1 + \hat{p}_1(t)\eta + \hat{p}_2(t)\eta^2], \quad (\text{A2})$$

where  $\eta = (1 - m/M)$  is the normalized mass with zero value at the ablation front,  $p_a$  is the ablation pressure, and  $M$  is the total shell mass. Second, a solution of Eq. (A1) is obtained near the ablation region as an expansion in  $\eta$ , assuming  $\eta \ll 1$ . And third, the adiabat is assumed to be determined by the early shock propagation through the shell and does not change significantly during the shell acceleration. The relation between the position and mass is determined by substituting

$$p(m, t) = \mu\alpha\rho^{5/3} \quad (\text{A3})$$

into the mass-conservation equation [here,  $\mu$  is defined in Eq. (19)]. The result is

$$\frac{\partial r^3}{\partial m} = \frac{3\mu^{3/5}}{4\pi} \left(\frac{\alpha}{\rho}\right)^{3/5}. \quad (\text{A4})$$

Next, the ablation pressure is written as a function of the ablation-front position  $R_a$ . Since the critical surface and the laser-deposition region move inward during the shell implosion, the ablation pressure (or drive pressure) increases with the shell convergence. Assuming that the ablation pressure scales with the laser intensity as  $p_a \sim I^{\beta_a}$ , the pressure change with the ablation-front radius  $R_a$  becomes  $p_a \sim (P_{\text{laser}}/R_a^2)^{\beta_a} = P_{\text{laser}}^{\beta_a} R_a^{-2\beta_a}$ , where  $P_{\text{laser}}$  is the laser power. The power index  $\beta_a$  depends on the details of the laser-absorption mechanism and thermal conduction (see, for example, Ref. 53). To generalize, we write the drive pressure as  $p_a \sim R_a^{-\beta}$ , where the values of the power index  $\beta$  typically ranges from 0.5 to 1.5 for various laser-deposition and thermal-conduction models and ablator materials. Introducing the normalized position  $\xi(\eta, t) = r(\eta, t)/R_0$ , where  $R_0$  is the ablation-front position at the beginning of the shell acceleration, the ablation pressure can be written as

$$p_a = p_{a0}\xi_a^{-\beta} \quad (\text{A5})$$

and Eq. (A4) takes the form

$$\frac{\partial \xi^3}{\partial \eta} = -\epsilon \xi_a^{3\beta/5} \left( \frac{\alpha/\alpha_a}{1 + \hat{p}_1\eta + \hat{p}_2\eta^2} \right)^{3/5}, \quad (\text{A6})$$

where  $\alpha_a$  is the shell adiabat in the ablation-front region, and  $\xi_a = R_a/R_0$ . The small parameter  $\epsilon$  is defined as

$$\epsilon = \frac{3\mu^{3/5}}{4\pi} \left( \frac{\alpha_a}{p_{a0}} \right)^{3/5} \frac{M_{\text{shell}}}{R_0^3} = \frac{M_{\text{shell}}}{4\pi\rho_{a0}R_0^3/3} \ll 1, \quad (\text{A7})$$

where  $p_{a0}$  and  $\rho_{a0}$  are the ablation pressure and the peak shell density at the beginning of shell acceleration, respectively. Keeping only the terms up to order of  $\eta$ , the solution of Eq. (A6) becomes

$$\xi(\eta, t) = \xi_a(t) \left[ 1 - \frac{\epsilon}{3} \xi_a(t)^{3\beta/5-3} \eta \right]. \quad (\text{A8})$$

Substituting Eq. (A8) back into Eq. (A1) determines the temporal evolution of the normalized ablation-front radius  $\xi_a$  and shell pressure  $p$

$$\xi_a'' = \frac{4\pi R_0}{M} p_{a0} \xi_a^{2-\beta} \hat{p}_1, \quad (\text{A9})$$

$$\hat{p}_2 = \frac{\epsilon}{6} \xi_a^{3/5\beta-3} \left[ \hat{p}_1 \left( 4 - \frac{3}{5}\beta \right) - \frac{M}{4\pi R_0 p_{a0}} \left( 2 - \frac{3}{5}\beta \right) \left( 3 - \frac{3}{5}\beta \right) \frac{\xi_a'^2}{\xi_a^{3-\beta}} \right]. \quad (\text{A10})$$

Assuming that the pressure at the inner shell surface ( $\eta = 1$ ) is  $p(\eta = 1) = p_{\text{bk}}(t)$  ( $p_{\text{bk}} \ll p_a$  during the shell acceleration) relates  $\hat{p}_2$  with  $\hat{p}_1$

$$\hat{p}_1 = -1 + p_{\text{bk}}/p_a - \hat{p}_2. \quad (\text{A11})$$

The shell pressure at the inner surface  $p_{\text{bk}}$  is determined from Eq. (30)

$$\frac{p_{\text{bk}}}{p_{a0}} \simeq \frac{\rho_{v0}}{\rho_0} \left\{ 1 + 2\sqrt{5} \left[ 1 - \left( \frac{\rho_{v0}}{\rho_0} \right)^{1/5} \right] \right\} \left( \frac{V_{\text{bk}0}}{V_{\text{bk}}} \right), \quad (\text{A12})$$

where  $V_{\text{bk}}$  and  $V_{\text{bk}0}$  are the volume surrounded by the inner surface of the shell and its value at the beginning of the shell acceleration, respectively. The volume ratio in Eq. (A12) is due to convergence effects. Then, Eq. (A10) gives

$$\hat{p}_2 = -\frac{\epsilon}{6} (4 - 3/5\beta) \xi_a^{3/5\beta-3} \times \frac{\xi_a'^2 / \xi_a^{3-\beta} C_\beta (M/4\pi R_0 p_{a0}) + 1 - p_{\text{bk}}/p_a}{1 + \epsilon(4 - 3/5\beta) \xi_a^{3/5\beta-3} / 6}, \quad (\text{A13})$$

where

$$C_\beta = \frac{(2 - 3/5\beta)(3 - 3/5\beta)}{4 - 3/5\beta}.$$

When the shell convergence is not significant ( $R_a \sim R_0$ ,  $\xi_a \sim 1$ ),  $\hat{p}_1 \simeq -1$ , and the ablation-front velocity, obtained by integrating Eq. (A9), reduces to

$$\xi_a'^2 = \frac{8\pi R_0 p_{a0}}{M} \frac{1 - \xi_a^{3-\beta}}{3 - \beta}. \quad (\text{A14})$$

Since the velocity gradient inside the shell is small at this stage in the implosion, the mass-averaged shell velocity  $v_{\text{shell}}$  can be approximated by the ablation-front velocity  $v_{\text{shell}} \simeq \dot{R}_a = R_0 \xi_a'$ . This gives the shell kinetic energy as a function of the ablation-front radius

$$\begin{aligned} \frac{M v_{\text{shell}}^2}{2} &= \frac{4\pi}{3 - \beta} [p_{a0} R_0^3 - p_a(t) R_a^3] \\ &= \frac{4\pi}{3 - \beta} p_{a0} R_0^3 \left[ 1 - \left( \frac{R_a}{R_0} \right)^{3-\beta} \right]. \end{aligned} \quad (\text{A15})$$

Equation (A15) shows, as expected, that as the shell converges and  $R_a$  gets smaller, the shell kinetic energy increases and the larger values of  $\beta$  [which correspond to a faster rise in the ablation pressure with convergence, see Eq. (A5)] lead to increased kinetic energy. Note that Eq. (A15) is not valid for  $\beta = 3$ . Integrating Eq. (A9) in this case leads to

$$\frac{M v_{\text{shell}}^2}{2} = 4\pi p_{a0} R_0^3 \ln \frac{R_0}{R_a}, \quad \beta = 3. \quad (\text{A16})$$

## APPENDIX B: MODEL OF SHELL DECELERATION

### 1. Equation for the hot-spot radius

Following the analysis used in modeling the shell acceleration [see Eqs. (A2)–(A10)], the pressure of the shocked shell is written as

$$p = p_{\text{hs}}(t) \left[ 1 + \hat{p}_1^{\text{hs}} \frac{m}{M} + \hat{p}_2^{\text{hs}} \left( \frac{m}{M} \right)^2 \right], \quad (\text{B1})$$

and the solution of Eq. (A1) is found near the inner surface of the shell as a series expansion in  $m/M \ll 1$ . If  $M_s$  is the mass of the shocked shell and the pressure at the shock front is  $p(M_s) = p_{\text{shock}}$ , substituting  $p_{\text{hs}}(t)$  from Eq. (25) into Eq. (B1) gives

$$\hat{p}_2^{\text{hs}} = -\frac{M}{6\rho_{\text{shock}0} V_{\text{hs}0}} \hat{p}_1^{\text{hs}}, \quad (\text{B2})$$

$$\hat{p}_1^{\text{hs}} = -(1 - p_{\text{shock}}/p_{\text{hs}}) \frac{M}{M_s} \left( 1 - \frac{M_s}{6\rho_{\text{shock}0} V_{\text{hs}0}} \right)^{-1}, \quad (\text{B3})$$

and the hot-spot radius is determined by

$$\ddot{R}_{\text{hs}} = S_{\text{hs}} \frac{p_{\text{hs}} - p_{\text{shock}}}{M_s} \left( 1 - \frac{M_s}{6\rho_{\text{shock}0} V_{\text{hs}0}} \right)^{-1}, \quad (\text{B4})$$

where  $S_{\text{hs}}$  is the surface area of the hot spot, and  $\rho_{\text{shock}0}$  and  $V_{\text{hs}0}$  are the shell density at the inner edge of the shell and the hot-spot volume at the beginning of the shell deceleration, respectively (see Fig. 21). As described earlier [see Eq. (26)], the maximum hot-spot pressure depends on the hot-spot convergence ratio during deceleration. Equation (B4) shows that the hot-spot convergence is determined by the pressure difference between the hot-spot and the shock fronts,  $p_{\text{hs}} - p_{\text{shock}}$ , and the shocked-shell mass (the

shocked mass  $M_s$ ). If the vapor pressure, for a given hot-spot radius, is increased in an experiment compared with the code predictions (due to the larger vapor mass, for example), then the shell deceleration is stronger and the shocked mass is smaller. This results in a smaller fraction of the shell kinetic energy being converted into the internal energy of the hot spot, leading to reduced hot-spot pressures.

## 2. Equations for the shocked mass and shock pressure

The conservation laws at the shock front are used to determine  $M_s$  and  $p_{\text{shock}}$ . The change in momentum of the shell material as it passes through the shock surface,  $-dM_s/dt(v_{\text{shell},s} - v_{\text{shock}})$ , is balanced by the pressure force  $-(p_{\text{shell},s} - p_{\text{shock}})S_{\text{shock}}$ , yielding

$$\frac{dM_s}{dt}(v_{\text{shell},s} - v_{\text{shock}}) = (p_{\text{shell},s} - p_{\text{shock}})S_{\text{shock}}, \quad (\text{B5})$$

where  $v_{\text{shock}}$ ,  $p_{\text{shock}}$  and  $v_{\text{shell},s} < 0$ ,  $p_{\text{shell},s}$  are the velocity and pressure at the shock front in the shock-compressed (region II in Fig. 22) and unshocked (region I in Fig. 22) regions, respectively, and  $S_{\text{shock}}$  is the surface area of the outgoing shock wave. The mass flux across the shock is determined from the Hugoniot relations,<sup>42</sup>

$$\frac{dM_s}{dt} = \sqrt{\frac{\rho_{\text{shell},s}}{3}} \sqrt{4p_{\text{shock}} + p_{\text{shell},s}} S_{\text{shock}}. \quad (\text{B6})$$

Eliminating  $dM_s/dt$  from Eqs. (B5) and (B6) gives

$$p_{\text{shock}} = p_{\text{shell},s} - \sqrt{\frac{\rho_{\text{shell},s}}{3}} (4p_{\text{shock},s} + p_{\text{shell},s})(v_{\text{shell},s} - v_{\text{shock}}). \quad (\text{B7})$$

The position of the outgoing shock wave,  $R_{\text{shock}}$ , is determined by

$$\frac{dR_{\text{shock}}}{dt} = \sqrt{\frac{4p_{\text{shock}} + p_{\text{shell},s}}{3\rho_{\text{shell},s}}} + v_{\text{shell},s}. \quad (\text{B8})$$

In the strong-shock approximation  $p_{\text{shock}} \gg p_{\text{shell}}$ , these equations reduce to

$$\begin{aligned} \frac{dM_s}{dt} &\simeq \frac{4}{3} \rho_{\text{shell},s} (v_{\text{shock}} - v_{\text{shell},s}) S_{\text{shock}}, \\ p_{\text{shock}} &\simeq \frac{4}{3} \rho_{\text{shell},s} (v_{\text{shock}} - v_{\text{shell},s})^2, \\ \frac{dR_{\text{shock}}}{dt} &= \frac{4}{3} v_{\text{shock}} - \frac{1}{3} v_{\text{shell},s}. \end{aligned} \quad (\text{B9})$$

The shock pressure  $p_{\text{shock}}$  continues to increase while the shell converges inward. This is a result of two effects: first, an increase in shell density ahead of the shock  $\rho_{\text{shell}}$  (because of the shell convergence); and second, a decrease in the absolute value of the post-shock velocity  $v_{\text{shock}}$  caused by the shell deceleration. The rate of increase in  $p_{\text{shock}}$  is

limited, however, by the deceleration of the unshocked shell and a reduction in  $|v_{\text{shell}}|$ . The shell density and pressure evolutions will be discussed next.

## 3. Equation for the unshocked shell density

Density evolution, according to the mass conservation equation, is determined by the fluid velocity gradient. The velocity gradient across the shell during acceleration is calculated by taking the time derivative of Eq. (A4)

$$\frac{1}{v} \frac{\partial v}{\partial m} = -\frac{2}{3\rho(m)V(m)} \left( 1 + \frac{3}{10} \frac{\partial p}{\partial t} \frac{r}{pv} \right). \quad (\text{B10})$$

Assuming that the velocity gradient is uniform across the shell, Eq. (B10) is evaluated at the ablation front. This gives an estimate of the velocity difference  $\Delta v$  across the shell

$$\frac{\Delta v}{vM} \simeq -\frac{2}{3\rho_a V_a} \left( 1 + \frac{3}{10} \frac{dp_a}{dR_a} \frac{R_a}{p_a} \right). \quad (\text{B11})$$

Equation (B11) shows that the velocity difference between the outer and inner parts of the shell is amplified during the implosion because of convergence ( $\rho_a V_a$  decreases). This effect is absent, for example, in planar geometry where the shell velocity profile is nearly flat. The ablation pressure scales with the ablation radius as  $p_a \sim R_a^{-\beta}$  [see Eq. (A5)], leading to  $dp_a/dR_a (R_a/p_a) = -\beta$ . Then, Eq. (43) is used in evaluating Eq. (B11) at the end of the ablation-front acceleration. This gives

$$\Delta v \simeq C_d c_s, \quad (\text{B12})$$

where  $C_d = \sqrt{2(2 - 3\beta/5)/(5 - \beta)}$ . For the values of  $\beta$  relevant to ICF implosions,  $\Delta v \simeq 0.8c_s - 0.9c_s$ . Equation (B12) shows that at the end of the ablation-front acceleration, the velocity variation across the shell is proportional to the shell sound speed. Thus, as the return shock starts propagating through the shell at the beginning of the shell deceleration, it first interacts with the inner part of the shell, which is moving inward with the larger velocity. Then, as the shock travels through the shell, the incoming shell velocity at the shock front decreases with time because of the velocity gradient shown in Eq. (B12). An additional decrease in the incoming shell velocity is caused by the pressure gradient that creates a force decelerating the unshocked shell.

To calculate the pressure gradient and the density evolution in the unshocked shell, the mass-conservation equation is used

$$\frac{\partial}{\partial t} \left( \frac{1}{\rho r^2} \right) = 4\pi \frac{\partial v}{\partial m}. \quad (\text{B13})$$

Then, substituting  $\partial v/\partial m \simeq \Delta v/M$  and using Eq. (B12) gives

$$\begin{aligned} \rho(m, t) &\simeq \rho_0(m) \left[ \frac{r_0(m)}{r(m, t)} \right]^2 \\ &\times \left[ 1 + 4\pi C_d \frac{c_{s0}}{M} (t - t_d) \rho_0(m) r_0(m)^2 \right]^{-1}, \end{aligned} \quad (\text{B14})$$

where  $c_{s0}$  is the shell sound speed at the beginning of deceleration,  $\rho_0(m)$  and  $r_0(m)$  are the shell density and position as functions of mass coordinate at the beginning of shell

deceleration, and  $t_d$  is the starting time of the shell deceleration. Strictly speaking, the velocity gradient  $\Delta v/M$  is not a constant. It increases during the shell deceleration because of the pressure gradient along the radial direction. This pressure gradient decelerates the ablation-front region, increasing  $\Delta v$ . Consequently, Eq. (B14) overestimates the density increase. Results of the hydrodynamic simulations indicate, however, that Eq. (B14) is accurate within a few-percent error.

#### 4. Equations for the unshocked shell velocity and pressure

The velocity slowdown ahead of the outgoing shock wave (region I in Fig. 22) is calculated using momentum-conservation equation  $dv_{\text{shell}}/dt \sim -S_{\text{shock}} \partial p / \partial m$ . Assuming that the shell adiabat does not change significantly inside the unshocked shell, the shell pressure is calculated by substituting Eq. (B14) into  $p \sim \rho^{5/3}$ . This gives

$$p_{\text{shell}} \simeq p_0(m) \left[ \frac{r_0(m)}{r(m,t)} \right]^{10/3} \Sigma^{-5/3},$$

$$\Sigma = 1 + 4\pi C_d \frac{c_{s0}}{M} (t - t_d) \rho_0(m) r_0(m)^2, \quad (\text{B15})$$

and the pressure gradient becomes

$$\frac{\partial p}{\partial m} \simeq \left( \frac{r_0}{r} \right)^{10/3} \Sigma^{-8/3} \left[ \frac{\partial p_0}{\partial m} + \frac{5p_0}{6\pi\rho_0 r_0^3} \right]$$

$$- \left( \frac{r_0}{r} \right)^{13/3} \Sigma^{-2/3} \frac{5p_0}{6\pi\rho_0 r_0^3}. \quad (\text{B16})$$

#### 5. Relation between the post-shock velocity and the hot-spot convergence rate

To complete defining the model for the shell deceleration and the hot-spot formation, the hot-spot convergence rate  $\dot{R}_{\text{hs}}$  must be related to the post-shock velocity  $v_{\text{shock}}$ . This is accomplished using the mass-conservation equation in the form shown in Eq. (B13). The shell density at the inner edge of the shell satisfies  $\rho_{\text{shell}} V_{\text{hs}} = \text{const}$  [because of the adiabatic approximation shown in Eq. (25)]. Therefore,

$$\frac{\dot{R}_{\text{hs}}}{3\rho_{\text{shock}0} V_{\text{hs}0}} \simeq \frac{v_{\text{shock}} - \dot{R}_{\text{hs}}}{M_s}, \quad (\text{B17})$$

and the shocked-shell velocity at the shock front becomes

$$v_{\text{shock}} = \dot{R}_{\text{hs}} \left( 1 + \frac{M_s}{3\rho_{\text{shock}0} V_{\text{hs}0}} \right). \quad (\text{B18})$$

Since  $\dot{R}_{\text{hs}} < 0$  prior to shell stagnation, Eq. (B18) shows that the velocity gradient is negative inside the shock-compressed region,  $v_{\text{shock}} - \dot{R}_{\text{hs}} < 0$ .

<sup>1</sup>J. D. Lindl, *Inertial Confinement Fusion* (Springer, New York, 1998).

<sup>2</sup>S. Atzeni and J. Meyer-Ter-Vehn, *The Physics of Inertial Fusion* (Clarendon Press, Oxford, 2004).

<sup>3</sup>R. Betti, K. Anderson, V. N. Goncharov, R. L. McCrory, D. D. Meyerhofer, S. Skupsky, and R. P. J. Town, *Phys. Plasmas* **9**, 2277 (2002).

<sup>4</sup>V. N. Goncharov, in *Laser-Plasma Interactions, Scottish Graduate Series*, edited by D. A. Jaroszynski, R. Bingham, and R. A. Cairns (CRC Press, Boca Raton, 2009), pp. 409–418.

<sup>5</sup>S. Chandrasekhar, *Hydrodynamic and Hydromagnetic Stability* (Clarendon, Oxford, 1961), p. 428.

<sup>6</sup>J. Sanz, *Phys. Rev. Lett.* **73**, 2700 (1994); V. N. Goncharov, R. Betti, R. L. McCrory, P. Sorotokin, and C. P. Verdon, *Phys. Plasmas* **3**, 1402 (1996).

<sup>7</sup>T. R. Boehly, D. L. Brown, R. S. Craxton, R. L. Keck, J. P. Knauer, J. H. Kelly, T. J. Kessler, S. A. Kumpan, S. J. Loucks, S. A. Letzring, F. J. Marshall, R. L. McCrory, S. F. B. Morse, W. Seka, J. M. Soures, and C. P. Verdon, *Opt. Commun.* **133**, 495 (1997).

<sup>8</sup>V. N. Goncharov, T. C. Sangster, T. R. Boehly, S. X. Hu, I. V. Igumenshchev, F. J. Marshall, R. L. McCrory, D. D. Meyerhofer, P. B. Radha, W. Seka, S. Skupsky, C. Stoeckl, D. T. Casey, J. A. Frenje, and R. D. Petrasso, *Phys. Rev. Lett.* **104**, 165001 (2010).

<sup>9</sup>J. Delettrez, R. Epstein, M. C. Richardson, P. A. Jaanimagi, and B. L. Henke, *Phys. Rev. A* **36**, 3926 (1987).

<sup>10</sup>V. N. Goncharov, T. C. Sangster, P. B. Radha, R. Betti, T. R. Boehly, T. J. B. Collins, R. S. Craxton, J. A. Delettrez, R. Epstein, V. Yu. Glebov, S. X. Hu, I. V. Igumenshchev, J. P. Knauer, S. J. Loucks, J. A. Marozas, F. J. Marshall, R. L. McCrory, P. W. McKenty, D. D. Meyerhofer, S. P. Regan, W. Seka, S. Skupsky, V. A. Smalyuk, J. M. Soures, C. Stoeckl, D. Shvarts, J. A. Frenje, R. D. Petrasso, C. K. Li, F. Seguin, W. Manheimer, and D. G. Colombant, *Phys. Plasmas* **15**, 056310 (2008).

<sup>11</sup>I. V. Igumenshchev, D. H. Edgell, V. N. Goncharov, J. A. Delettrez, A. V. Maximov, J. F. Myatt, W. Seka, A. Shvydky, S. Skupsky, and C. Stoeckl, *Phys. Plasmas* **17**, 122708 (2010).

<sup>12</sup>I. V. Igumenshchev, W. Seka, D. H. Edgell, D. T. Michel, D. H. Froula, V. N. Goncharov, R. S. Craxton, L. Divol, R. Epstein, R. Follett, J. H. Kelly, T. Z. Kosc, A. V. Maximov, R. L. McCrory, D. D. Meyerhofer, P. Michel, J. F. Myatt, T. C. Sangster, A. Shvydky, S. Skupsky, and C. Stoeckl, *Phys. Plasmas* **19**, 056314 (2012).

<sup>13</sup>C. J. Randall, J. R. Albritton, and J. J. Thomson, *Phys. Fluids* **24**, 1474 (1981).

<sup>14</sup>W. L. Kruer, *The Physics of Laser-Plasma Interactions, Frontiers in Physics* Vol. 73, edited by D. Pines (Addison-Wesley, Redwood City, CA, 1988).

<sup>15</sup>A. Simon, R. W. Short, E. A. Williams, and T. Dewandre, *Phys. Fluids* **26**, 3107 (1983).

<sup>16</sup>D. T. Michel, A. V. Maximov, R. W. Short, S. X. Hu, J. F. Myatt, W. Seka, A. A. Solodov, B. Yaakobi, and D. H. Froula, *Phys. Rev. Lett.* **109**, 155007 (2012).

<sup>17</sup>J. Myatt, H. X. Vu, D. F. DuBois, D. A. Russell, J. Zhang, R. W. Short, and A. V. Maximov, *Phys. Plasmas* **20**, 052705 (2013).

<sup>18</sup>W. M. Manheimer and D. C. Colombant, *Phys. Fluids* **25**, 1644 (1982).

<sup>19</sup>D. T. Michel, C. Sorce, R. Epstein, N. Whiting, I. V. Igumenshchev, R. Jungquist, and D. H. Froula, *Rev. Sci. Instrum.* **83**, 10E530 (2012).

<sup>20</sup>W. H. Ye, L. F. Wang, and X. T. He, *Phys. Plasmas* **17**, 122704 (2010).

<sup>21</sup>P. B. Radha, V. N. Goncharov, T. J. B. Collins, J. A. Delettrez, Y. Elbaz, V. Yu. Glebov, R. L. Keck, D. E. Keller, J. P. Knauer, J. A. Marozas, F. J. Marshall, P. W. McKenty, D. D. Meyerhofer, S. P. Regan, T. C. Sangster, D. Shvarts, S. Skupsky, Y. Srebro, R. P. J. Town, and C. Stoeckl, *Phys. Plasmas* **12**, 032702 (2005).

<sup>22</sup>J. J. MacFarlane, I. E. Golovkin, P. Wang, P. R. Woodruff, and N. A. Pereyra, *High Energy Density Phys.* **3**, 181 (2007).

<sup>23</sup>D. T. Michel, V. N. Goncharov, I. V. Igumenshchev, R. Epstein, and D. H. Froula, *Phys. Rev. Lett.* **111**, 245005 (2013).

<sup>24</sup>W. Seka, D. H. Edgell, J. P. Knauer, J. F. Myatt, A. V. Maximov, R. W. Short, T. C. Sangster, C. Stoeckl, R. E. Bahr, R. S. Craxton, J. A. Delettrez, V. N. Goncharov, I. V. Igumenshchev, and D. Shvarts, *Phys. Plasmas* **15**, 056312 (2008).

<sup>25</sup>T. Dewandre, J. R. Albritton, and E. A. Williams, *Phys. Fluids* **24**, 528 (1981).

<sup>26</sup>S. Skupsky, R. W. Short, T. Kessler, R. S. Craxton, S. Letzring, and J. M. Soures, *J. Appl. Phys.* **66**, 3456 (1989).

<sup>27</sup>See National Technical Information Service Document No. DOE/SF/19460-335 [Laboratory for Laser Energetics LLE Review **130**, 72, (2012)]. Copies may be obtained from the National Technical Information Service, Springfield, VA 22161.

<sup>28</sup>V. N. Goncharov, in *Laser-Plasma Interactions and Applications, Scottish Graduate Series*, edited by P. McKenna, D. Neely, R. Bingham, and D. A. Jaroszynski (Springer, 2013), pp. 135–183.

<sup>29</sup>H. Brysk, *Plasma Phys.* **15**, 611 (1973).



- <sup>30</sup>T. C. Sangster, V. N. Goncharov, R. Betti, P. B. Radha, T. R. Boehly, D. T. Casey, T. J. B. Collins, R. S. Craxton, J. A. Delettrez, D. H. Edgell, R. Epstein, C. J. Forrest, J. A. Frenje, D. H. Froula, M. Gatu-Johnson, V. Yu. Glebov, D. R. Harding, M. Hohenberger, S. X. Hu, I. V. Igumenshchev, R. Janezic, J. H. Kelly, T. J. Kessler, C. Kingsley, T. Z. Kosc, J. P. Knauer, S. J. Loucks, J. A. Marozas, F. J. Marshall, A. V. Maximov, R. L. McCrory, P. W. McKenty, D. D. Meyerhofer, D. T. Michel, J. F. Myatt, R. D. Petrasso, S. P. Regan, W. Seka, W. T. Shmayda, R. W. Short, A. Shvydky, S. Skupsky, J. M. Soures, C. Stoeckl, W. Theobald, V. Versteeg, B. Yaakobi, and J. D. Zuegel, *Phys. Plasmas* **20**, 056317 (2013).
- <sup>31</sup>J. A. Frenje, C. K. Li, F. H. Seguin, D. T. Casey, R. D. Petrasso, T. C. Sangster, R. Betti, V. Yu. Glebov, and D. D. Meyerhofer, *Phys. Plasmas* **16**, 042704 (2009); J. A. Frenje, D. T. Casey, C. K. Li, F. H. Seguin, R. D. Petrasso, V. Yu. Glebov, P. B. Radha, T. C. Sangster, D. D. Meyerhofer, S. P. Hatchett, S. W. Haan, C. J. Cerjan, O. L. Landen, K. A. Fletcher, and R. J. Leeper, *ibid.* **17**, 056311 (2010).
- <sup>32</sup>C. Forrest, P. B. Radha, V. Yu. Glebov, V. N. Goncharov, J. P. Knauer, A. Pruyne, M. Romanofsky, T. C. Sangster, M. J. Shoup III, C. Stoeckl, D. T. Casey, M. Gatu-Johnson, and S. Gardner, *Rev. Sci. Instrum.* **83**, 10D919 (2012).
- <sup>33</sup>C. Stoeckl, V. Yu. Glebov, S. Roberts, T. C. Sangster, R. A. Lerche, R. L. Griffith, and C. Source, *Rev. Sci. Instrum.* **74**, 1713 (2003).
- <sup>34</sup>R. Betti and C. Zhou, *Phys. Plasmas* **12**, 110702 (2005).
- <sup>35</sup>C. Cerjan, P. T. Springer, and S. M. Sepke, *Phys. Plasmas* **20**, 056319 (2013).
- <sup>36</sup>S. X. Hu, P. B. Radha, and V. N. Goncharov, *Bull. Am. Phys. Soc.* **58**, 324 (2013).
- <sup>37</sup>F. J. Marshall and J. A. Oertel, *Rev. Sci. Instrum.* **68**, 735 (1997).
- <sup>38</sup>M. J. Edwards, P. K. Patel, J. D. Lindl, L. J. Atherton, S. H. Glenzer, S. W. Haan, J. D. Kilkenny, O. L. Landen, E. I. Moses, A. Nikroo, R. Petrasso, T. C. Sangster, P. T. Springer, S. Batha, R. Benedetti, L. Bernstein, R. Betti, D. L. Bleuel, T. R. Boehly, D. K. Bradley, J. A. Caggiano, D. A. Callahan, P. M. Celliers, C. J. Cerjan, K. C. Chen, D. S. Clark, G. W. Collins, E. L. Dewald, L. Divol, S. Dixit, T. Doepfner, D. H. Edgell, J. E. Fair, M. Farrell, R. J. Fortner, J. Frenje, M. G. Gatu Johnson, E. Giraldez, V. Yu. Glebov, G. Grim, B. A. Hammel, A. V. Hamza, D. R. Harding, S. P. Hatchett, N. Hein, H. W. Herrmann, D. Hicks, D. E. Hinkel, M. Hoppe, W. W. Hsing, N. Izumi, B. Jacoby, O. S. Jones, D. Kalantar, R. Kauffman, J. L. Kline, J. P. Knauer, J. A. Koch, B. J. Koziolowski, G. Kyrala, K. N. LaFortune, S. Le Pape, R. J. Leeper, R. Lerche, T. Ma, B. J. MacGowan, A. J. MacKinnon, A. Macphee, E. R. Mapoles, M. M. Marinak, M. Mauldin, P. W. McKenty, M. Meezan, P. A. Michel, J. Milovich, J. D. Moody, M. Moran, D. H. Munro, C. L. Olson, K. Opachich, A. E. Pak, T. Parham, H.-S. Park, J. E. Ralph, S. P. Regan, B. Remington, H. Rinderknecht, H. F. Robey, M. Rosen, S. Ross, J. D. Salmonson, J. Sater, D. H. Schneider, F. H. Sèguin, S. M. Sepke, D. A. Shaughnessy, V. A. Smalyuk, B. K. Spears, C. Stoeckl, W. Stoeffl, L. Suter, C. A. Thomas, R. Tommasini, R. P. Town, S. V. Weber, P. J. Wegner, K. Widman, M. Wilke, D. C. Wilson, C. B. Yeamans, and A. Zylstra, *Phys. Plasmas* **20**, 070501 (2013).
- <sup>39</sup>J. A. Paisner, J. D. Boyes, S. A. Kumpan, W. H. Lowdermilk, and M. S. Sorem, *Laser Focus World* **30**, 75 (1994).
- <sup>40</sup>G. Guderley, *Luftfahrtforschung* **19**, 302 (1942).
- <sup>41</sup>C. Bellei, P. A. Amendt, S. C. Wilks, M. G. Haines, D. T. Casey, C. K. Li, R. Petrasso, and D. R. Welch, *Phys. Plasmas* **20**, 012701 (2013); C. Bellei, P. A. Amendt, S. C. Wilks, D. T. Casey, C. K. Li, R. Petrasso, and D. R. Welch, *ibid.* **20**, 044702 (2013).
- <sup>42</sup>L. D. Landau and L. M. Lifshitz, *Fluid Mechanics* (Pergamon, New York, 1982).
- <sup>43</sup>I. V. Igumenshchev, V. N. Goncharov, W. T. Shmayda, D. R. Harding, T. C. Sangster, and D. D. Meyerhofer, *Phys. Plasmas* **20**, 082703 (2013).
- <sup>44</sup>R. Betti and J. Sanz, *Phys. Rev. Lett.* **97**, 205002 (2006).
- <sup>45</sup>D. Layzer, *Astrophys. J.* **122**, 1 (1955); D. Oron, L. Arazi, D. Kartoon, A. Rikanati, U. Alon, and D. Shvarts, *Phys. Plasmas* **8**, 2883 (2001); V. N. Goncharov, *Phys. Rev. Lett.* **88**, 134502 (2002).
- <sup>46</sup>D. H. Edgell, W. Seka, R. E. Bahr, T. R. Boehly, and M. J. Bonino, *Phys. Plasmas* **15**, 092704 (2008).
- <sup>47</sup>M. C. Herrmann, M. Tabak, and J. D. Lindl, *Phys. Plasmas* **8**, 2296 (2001).
- <sup>48</sup>A. Bhagatwala and S. K. Lele, *Phys. Fluids* **24**, 085102 (2012).
- <sup>49</sup>I. V. Igumenshchev, D. H. Froula, D. H. Edgell, V. N. Goncharov, T. J. Kessler, F. J. Marshall, R. L. McCrory, P. W. McKenty, D. D. Meyerhofer, D. T. Michel, T. C. Sangster, W. Seka, and S. Skupsky, *Phys. Rev. Lett.* **110**, 145001 (2013); D. H. Froula, T. J. Kessler, I. V. Igumenshchev, R. Betti, V. N. Goncharov, H. Huang, S. X. Hu, E. Hill, J. H. Kelly, D. D. Meyerhofer, A. Shvydky, and J. D. Zuegel, *Phys. Plasmas* **20**, 082704 (2013).
- <sup>50</sup>S. E. Bodner, D. G. Colombant, A. J. Schmitt, and M. Klapisch, *Phys. Plasmas* **7**, 2298 (2000).
- <sup>51</sup>S. X. Hu, G. Fiksel, V. N. Goncharov, S. Skupsky, D. D. Meyerhofer, and V. A. Smalyuk, *Phys. Rev. Lett.* **108**, 195003 (2012); G. Fiksel, S. X. Hu, V. N. Goncharov, D. D. Meyerhofer, T. C. Sangster, V. A. Smalyuk, B. Yaakobi, M. J. Bonino, and R. Jungquist, *Phys. Plasmas* **19**, 062704 (2012).
- <sup>52</sup>R. J. Henchen, *Bull. Am. Phys. Soc.* **58**, 151 (2013).
- <sup>53</sup>C. E. Max, C. F. McKee, and W. C. Mead, *Phys. Fluids* **23**, 1620 (1980).